An experimental study on characterization of physical properties of ultramafic rocks and controls on evolution of fracture permeability during serpentinization at hydrothermal conditions

Aida Farough

Dissertation submitted to the faculty of the Virginia Polytechnic Institute and State University in partial fulfillment of the requirements for the degree of

Doctor of Philosophy
In
Geosciences

Robert P. Lowell, Chair
Robert J. Bodnar
Mark J. Caddick
John A. Hole
J. Donald Rimstidt

August 13th, 2015
Blacksburg, VA

Keywords: Ultramafic Rocks, Serpentinization, Fracture Permeability, Intact Permeability, Pressure dependency, olivine transformation

An experimental study on characterization of physical properties of ultramafic rocks and controls on evolution of fracture permeability during serpentinization at hydrothermal conditions

Aida Farough

ABSTRACT

Serpentinization is a complex set of hydration reactions, where olivine and pyroxene are replaced by serpentine, magnetite, brucite, talc and carbonate minerals. Serpentinization reactions alter chemical, mechanical, magnetic, seismic, and hydraulic properties of the crust. To understand the complicated nature of serpentinization and the linkages between physical and chemical changes during the reactions, I performed flow-through laboratory experiments on cylindrically cored samples of ultramafic rocks.

Each core had a well-mated through-going tensile fracture, to investigate evolution of fracture permeability during serpentinization. The samples were tested in a triaxial loading machine at an effective pressure of 30 MPa, and temperature of 260°C, simulating a depth of 2 km under hydrostatic conditions. Fracture permeability decreased by one to two orders of magnitude during the 200 to 340 hour experiments. Electron microprobe and SEM data indicated the formation of needle-shaped crystals of serpentine composition along the walls of the fracture, and chemical analyses of sampled pore fluids were consistent with dissolution of ferro-magnesian minerals. The rate of transformation of olivine to serpentine in a tensile fracture is calculated using the data on evolution of fracture permeability assuming the fracture permeability could be represented by parallel plates. Assuming the dissolution and precipitation reactions occur simultaneously; the rate of transformation at the beginning of the experiments was ~ 10^{-8}-10^{-9} (mol/m^2s) and decreased monotonically by about an order of magnitude towards

the end of the experiment. Results show that dissolution and precipitation is the main mechanism contributing to the reduction in fracture aperture. The experimental results suggest that the fracture network in long-lived hydrothermal circulation systems may be sealed rapidly as a result of mineral precipitation, and generation of new permeability resulting from a combination of tectonic and crystallization-induced stresses may be required to maintain fluid circulation.

Another set of flow through experiments were performed on intact samples of ultramafic rocks at room temperature and effective pressures of 10, 20 and 30 MPa to estimate the pressure dependency of intact permeability. Porosity and density measurements were also performed with the purpose of characterizing these properties of ultramafic rocks.

The pressure dependency of the coefficient of matrix permeability of the ultramafic rock samples fell in the range of 0.05-0.14 MPa^{-1}. Using porosity and permeability measurements, the ratio of interconnected porosity to total porosity was estimated to be small and the permeability of the samples was dominantly controlled by microcracks. Using the density and porosity measurements, the degree of alteration of samples was estimated. Samples with high density and pressure dependent permeability had a smaller degree of alteration than those with lower density and pressure dependency.

ACKNOWLEDGEMENTS

I would like to express my sincere gratitude to my advisor Dr. Robert P. Lowell for the continuous support of my research, for his patience, motivation, enthusiasm and immense knowledge. His guidance helped me in all aspects of this research and writing of this dissertation. I could not have imagined having a better advisor and mentor through my graduate studies.

Besides my advisor, I would like to thank the rest of my committee: Dr. Robert J. Bodnar, Dr. Mark J. Caddick, Dr. John A. Hole and Dr. J. Donald Rimstidt for their guidance and insightful comments, suggestions and support in the last 3 years.

My sincere thanks also goes to Dr. David A. Lockner and Dr. Diane E. Moore, for offering me the opportunity to work with them at the rock physics laboratories at the United States Geological Survey in Menlo Park, CA. They generously devoted their time, knowledge, and equipment to my project; and for that I will forever be thankful. I also thank Lee-gray Boze for helping me in preparations for experiments.

I would like to thank Dr. Neil Johnson and Dr. Luca Fedele for training me in using XRD, Microprobe and SEM. I also thank Dr. Esther Schwarzenbach and Dr. James Beard for helping me with analysis and interpretation of the results.

I would like to express my warm thanks and love to my parents, Hadi Farough and Farangis Kousha, whom her memory will forever be with me, and my sisters, Atoussa and Samira Farough, for believing in me and for their unconditional love, encouragement, and support. I also deeply appreciate the support of my extended family, especially my aunts, Farahnaz Kousha and Soraya Farough and brothers in Law, Amir Alemzadeh and Taha Gholipour.

Lastly, I offer my regards and blessings to all of my friends, my officemates in Derring 1070, the geophysics group and the faculty and staff of the department of Geosciences for their emotional support during the completion of my degree, especially: Pavithra Sekhar, Narges Dorratoltaj, Kannikha Kolandaivelu, Claudia Adam, Aaron Prunty, Aida Nourbakhsh, Kate Craft and Sharmin Shamsalsadati.

This work was supported in part by John K. Costain graduate geophysics endowed scholarship and Aubrey E. Orange endowed award in geophysics from department of Geosciences at Virginia Tech, Roundtable "Make A Difference" scholarship from college of Science at Virginia Tech, graduate student research grant from Geological Society of America, and NSF Grant OCE-1131471 to RPL.

Table of Contents

List of Figures

Chapter 2:

Chapter 3:

List of Tables

Chapter 1: Introduction

To understand fluid-rock interactions in the oceanic crust, knowledge of transport properties of rocks, especially porosity and permeability, is essential. Water-rock interactions alter physical and chemical properties of the host rock and seawater. Study of the chemistry of hydrothermal vent fluids at slow and ultraslow spreading ridges often shows evidence of chemical reactions between seawater and peridotite [e.g., *Charlou et al.*, 1991; *Rona et al*., 1992; *Charlou and Donval*, 1993; *Bougault et al.*, 1998; *Gracia et al.*, 2000; *Schmidt et al.*, 2007].

One of the most complex chemical reactions between seawater and ultramafic rocks is serpentinization. During serpentinization reactions, olivine and pyroxene are replaced by serpentine, magnetite, brucite, talc and carbonate minerals while methane, hydrogen and silica go into solution. In addition to releasing heat and altering rock and fluid chemistry, serpentinization reactions are accompanied by volume expansion ranging between 25%-45% [*Coleman*, 1971].

As a result of the recognized importance of serpentinization in a wide variety of tectonic environments and its far-reaching impact on geodynamical, geophysical, geochemical, and biological processes, there have been numerous studies on serpentinization reactions in natural settings [e.g., *Bach et al.*, 2004, 2006; *Frost and Beard*, 2007; *Beard et al.*, 2009] and in laboratory environments. Experimental studies on serpentinization have been categorized as [modified from *Ogasawara et al.* 2013]: (1) those focusing primarily on the rate and extent of reaction [e.g., *Wegner and Ernst*, 1983; *Okamoto et al.*, 2011; *Lafay et al.*, 2012; *Malvoisin et al.*, 2012; *Martin and Fyfe*,1970], (2) those focusing on the evolution of fluid chemistry [e.g., *Seyfried and Dibble*, 1980; *Janecky and Seyfried*, 1986; *Allen and Seyfried*, 2003; *Seyfried et al.*, 2007; *Normand et al.* 2002; *Godard et al.* 2013], (3) those focusing on the production of H_2 and

hydrocarbons [e.g., *Berndt et al.*, 1996; *McCollom and Seewald*, 2001; *Andreani et al*., 2009; *Jones et al*., 2010; *Marcaillou et al*., 2011; *Hövelmann et al*., 2012] and (4) those focusing on the permeability of serpentine-bearing rocks and its evolution during serpentinization [*MacDonald and Fyfe*, 1985; *Hirose and Hayman*, 2008; *Godard et al*., 2013; *Andreani et al.*, 2009; *Farough et al.*, 2015].

Despite the importance of serpentinization reactions on deformation, crustal evolution, and geochemical cycling, the linkage between physical and chemical changes during serpentinization reactions is not well understood. To better understand the evolution of permeability, porosity, rock mineralogy, and fluid chemistry during serpentinization reactions and the linkages between the chemical reactions and physical changes, I performed a number of flow-through experiments on natural samples of ultramafic rocks with different bulk compositions.

One set of experiments was performed at constant high pressure and temperature conditions, at which the kinetics of serpentinization reactions are high, on rock cores with a single axial through going tensile fracture and another set of experiments was performed at variable high pressures and room temperature on intact cores to estimate intact permeability and pressure dependency of physical properties of ultramafic rocks.

Chapter 2 is focused on evolution of fracture permeability of ultramafic rocks undergoing serpentinization at hydrothermal conditions. In chapter 3 an analytical model is developed for estimating rate of transformation of forsterite and enstatite to serpentine for an experimental study on evolution of fracture permeability in ultramafic rocks at hydrothermal conditions. Physical properties of some ultramafic rocks, permeability as a function of pressure, porosity-permeability relationship and density-degree of alteration relationship are topic of chapter 4.

1. References

Allen, D. E., and W. E. Seyfried (2003), Compositional controls on vent fluids from ultramafic-hosted hydrothermal systems at mid-ocean ridges: An experimental study at 400°C, 500 bars, *Geochimica et Cosmochimica Acta*, *67*(8), 1531-1542.

Andreani, M., L. Luquot, P. Gouze, M. Godard, E. Hoise, and B. Gibert (2009), Experimental study of carbon sequestration reactions controlled by the percolation of CO_2-rich brine through peridotites, *Environmental Science & Technology*, *43*(4), 1226-1231.

Bach, W., C. J. Garrido, H. Paulick, D. J. Harvey, and M. Rosner (2004), Seawater-peridotite interactions: First insights from ODP Leg 209, MAR 15°N, *Geochemistry Geophysics Geosystems*, *5*, Q09F26, doi:10.1029/2004GC000744.

Bach, W., H. Paulick, C. J. Garrido, B. Ildefonse, W. P. Meurer, and S. E. Humphris (2006), Unraveling the sequence of serpentinization reactions: petrography, mineral chemistry, and petrophysics of serpentinites from MAR 15°N (ODP Leg 209, Site 1274), *Geophysical Research Letters*, *33*, L13306, doi:10.1029/2006GL025681.

Beard, J. S., B. R. Frost, P. Fryer, A. McCaig, R. Searle, B. Ildefonse, P. Zinin, and S. K. Sharma (2009), Onset and Progression of Serpentinization and Magnetite Formation in Olivine-rich Troctolite from IODP Hole U1309D, *Journal of Petrology*, *50*(3), 387-403.

Berndt, M. E., R. R. Seal II, W. C. Shanks III, and W. E. S. J. (1996), Hydrogen isotope systematics of phase separation in submarine hydrothermal systems: Experimental calibration and theoretical models, *Geochimica et Cosmochimica Acta*, *60*, 1595-1604.

Bougault, H., M. Aballea, J. Radford-Knoery, J. L. Charlou, P. Jean Baptiste, P. Appriou, H. D. Needham, C. German, and M. Miranda (1998), FAMOUS and AMAR segments on the Mid-

Atlantic Ridge: ubiquitous hydrothermal Mn, CH 4, δ 3 He signals along the rift valley walls and rift offsets, *Earth and Planetary Science Letters*, *161*, 1-17.

Charlou, J.L., and J.P. Donval (1993), Hydrothermal methane venting between 12 N and 26 N along the Mid-Atlantic Ridge, *Journal of Geophysical Research*, *98*(B6), 9625-9642.

Charlou, J. L., H. Bougault, P. Appriou, T. Nelsen, and P. Rona (1991), Different TDM/CH4 hydrothermal plume signatures: TAG site at 26°N and serpentinized ultrabasic diapir at 15°05′N on the Mid-Atlantic Ridge, *Geochimica et Cosmochimica Acta*, *55*(11), 3209-3222.

Coleman, R. G. (1971), Petrologic and geophysical nature of serpentinites, *Geological Society of America Bulletin*, *82*(4), 897-918.

Farough, A., D. E. Moore, D. A. Lockner, R. P. Lowell (2015), Evolution of fracture permeability of ultramafic rocks undergoing serpentinization at hydrothermal conditions: An experimental study, *Geochemistry Geophysics Geosystems*, under review.

Frost, B. R., and J. S. Beard (2007), On Silica Activity and Serpentinization, *Journal of Petrology*, *48*(7), 1351-1368.

Gràcia, E., J. L. Charlou, J. Radford-Knoery, and L. M. Parson (2000), Non-transform offsets along the Mid-Atlantic Ridge south of the Azores (38 N–34 N): ultramafic exposures and hosting of hydrothermal vents, *Earth and Planetary Science Letters*, *177*(1), 89-103.

Godard, M., L. Luquot, M. Andreani, and P. Gouze (2013), Incipient hydration of mantle lithosphere at ridges: A reactive-percolation experiment, *Earth and Planetary Science Letters*, *371–372*(0), 92-102.

Hövelmann, J., H. Austrheim, and B. Jamtveit (2012), Microstructure and porosity evolution during experimental carbonation of a natural peridotite, *Chemical Geology*, *334*, 254-265.

Hirose, T., and N. Hayman (2008), Structure, permeability, and strength of a fault zone in the footwall of an oceanic core complex, the Central Dome of the Atlantis Massif, Mid-Atlantic Ridge, 30°N, *Journal of Structural Geology, 30*, 1060-1071.

Janecky, D., and W. Seyfried Jr (1986), Hydrothermal serpentinization of peridotite within the oceanic crust: experimental investigations of mineralogy and major element chemistry, *Geochimica et Cosmochimica Acta, 50*(7), 1357-1378.

Jones, L., C. Oze, J. Goldsmith, and R. Rosenbauer (2010), Catalysis of Methane Production in Serpentinization Systems, In *AGU Fall Meeting Abstracts*, vol. 1, p. 1475. 2010.

Lafay, R., G. Montes-Hernandez, E. Janots, R. Chiriac, N. Findling, and F. Toche (2012), Mineral replacement rate of olivine by chrysotile and brucite under high alkaline conditions, *Journal of Crystal Growth, 347*(1), 62-72.

Macdonald, A., and W. Fyfe (1985), Rate of serpentinization in seafloor environments, *Tectonophysics, 116*(1), 123-135.

Malvoisin, B., F. Brunet, J. Carlut, S. Rouméjon, and M. Cannat (2012), Serpentinization of oceanic peridotites: 2. Kinetics and processes of San Carlos olivine hydrothermal alteration, *Journal of Geophysical Research: 117*(B4), B04102, doi:10.1029/2011JB008842.

Marcaillou, C., M. Munoz, O. Vidal, T. Parra, and M. Harfouche (2011), Mineralogical evidence for H2 degassing during serpentinization at 300° C/300bar, *Earth and Planetary Science Letters*, *303*(3), 281-290.

Martin, B., and W. Fyfe (1970), Some experimental and theoretical observations on the kinetics of hydration reactions with particular reference to serpentinization, *Chemical Geology, 6*, 185-202.

McCollom, T. M., and J. S. Seewald (2001), A reassessment of the potential for reduction of dissolved CO2 to hydrocarbons during serpentinization of olivine, *Geochimica et Cosmochimica Acta*, *65*(21), 3769-3778.

Normand, C. (2002), Hydrothermal alteration of olivine in a flow-through autoclave: Nucleation and growth of serpentine phases, *The American mineralogist*, *87*(11-12), 1699-1709.

Ogasawara, Y., A. Okamoto, N. Hirano, and N. Tsuchiya (2013), Coupled reactions and silica diffusion during serpentinization, *Geochimica et Cosmochimica Acta*, *119*, 212-230.

Okamoto, A., Y. Ogasawara, Y. Ogawa, and N. Tsuchiya (2011), Progress of hydration reactions in olivine–H_2O and orthopyroxenite–H_2O systems at 250˚C and vapor-saturated pressure, *Chemical Geology*, *289*(3–4), 245-255.

Rona, B., Charlou, Appriou, Nelsen, Trefry, Eberhart, BArone, Needham (1992), Hydrothermal circulation, serpentinization, and degassing at a rift valley-fracture zone intersection: MAR near 15N, 45W, *Geology*, *20*, 783-786.

Schmidt, K., A. Koschinsky, D. Garbeschonberg, L. Decarvalho, and R. Seifert (2007), Geochemistry of hydrothermal fluids from the ultramafic-hosted Logatchev hydrothermal field, 15°N on the Mid-Atlantic Ridge: Temporal and spatial investigation, *Chemical Geology*, *242*(1-2), 1-21.

Seyfried Jr, W., and W. Dibble Jr (1980), Seawater-peridotite interaction at 300 C and 500 bars: implications for the origin of oceanic serpentinites, *Geochimica et Cosmochimica Acta*, *44*(2), 309-321.

Seyfried, W. E., D. I. Foustoukos, and Q. Fu (2007), Redox evolution and mass transfer during serpentinization: An experimental and theoretical study at 200°C, 500bar with implications

for ultramafic-hosted hydrothermal systems at Mid-Ocean Ridges, *Geochimica et Cosmochimica Acta*, *71*(15), 3872-3886.

Wegner, W. W., and W. Ernst (1983), Experimentally determined hydration and dehydration reaction rates in the system MgO–SiO2–H2O, *American Journal of Science*, *283*, 151-180.

Chapter 2: Evolution of Fracture Permeability of Ultramafic Rocks Undergoing Serpentinization at Hydrothermal Conditions: An Experimental Study

Farough, A.[1], D. E. Moore[2], D. A. Lockner[2], R. P. Lowell[1],

[1] Department of Geosciences, Virginia Tech, Blacksburg, VA

[2] US Geological Survey, Menlo Park, CA

Corresponding author: afarough@vt.edu

Key words: Fracture permeability, Serpentinization, Water-rock interaction, Hydrothermal, Fault zone

---

Abstract

We performed flow-through laboratory experiments on 5 cylindrically cored samples of ultramafic rocks, in which we generated a well-mated through-going tensile fracture, to investigate evolution of fracture permeability during serpentinization. The samples were tested in a triaxial loading machine at a confining pressure of 50 MPa, pore pressure of 20 MPa, and temperature of 260°C, simulating a depth of 2 km under hydrostatic conditions. A pore-pressure difference of approximately 2 MPa was imposed across the ends of the sample. Fracture permeability decreased by one to two orders of magnitude during the 200 to 340 hour experiments. Electron microprobe and SEM data indicated the formation of needle-shaped crystals of serpentine composition along the walls of the fracture, and chemical analyses of sampled pore fluids were consistent with dissolution of ferro-magnesian minerals. By comparing the difference between fracture permeability and matrix permeability measured on intact samples of the same rock types, we concluded that the contribution of the low matrix permeability to flow is negligible and essentially all of the flow is focused in the tensile fracture. The experimental results suggest that the fracture network in long-lived hydrothermal circulation systems can be sealed rapidly as a result of mineral precipitation, and generation of new permeability resulting from a combination of tectonic and crystallization-induced stresses is required to maintain fluid circulation.

1. Introduction

The permeability of fractured rocks and its temporal evolution are of critical importance for understanding hydrothermal processes in oceanic crust near and away from oceanic spreading centers. At many of the high temperature hydrothermal systems located on slow and ultra-slow spreading ridges, such as Rainbow and Logatchev vent fields on the Mid-Atlantic Ridge (MAR) [e.g. *Batuyev et al.*, 1994; *Bogdanov et al.*, 1995], and on Southwest Indian Ridge [*Bach et al.*, 2002], fluids are transported in part through ultramafic rocks. The Lost City Hydrothermal Field located on 1.5 Ma crust on the Atlantis Massif (AM) [e.g., *Kelley et al.* 2001], and the recently discovered Von Damm Hydrothermal Field near the Mid-Cayman Spreading Center [*Connelly et al.*, 2012] represent a class of off-axis circulation systems that emanate fluids at low temperatures. The permeability required to allow such vigorous circulation is estimated to be ~10^{-12}–10^{-14} m^2 [e.g., *Lowell et al.*, 2013], indicating that permeability is governed by faults and fractures.

As fluid circulates through fractures in ultramafic rocks, it promotes a set of hydration reactions in the host rock, commonly referred to as serpentinization, that play important roles in the structure of oceanic crust [e.g. *Cann et al.*, 1997; *Escartin et al*., 2001]. During serpentinization olivine and pyroxene are replaced by serpentine, magnetite, brucite, talc and carbonate minerals, thus altering the chemical, mechanical, magnetic, seismic, and hydraulic properties of the crust [e.g., *Carlson*, 2001; *Cannat*, 1993]. A key feature of these reactions is volume expansion [e.g., *Coleman*, 1971; *O'Hanley*, 1992], which tends to reduce porosity and permeability and inhibit fluid circulation. Thus it seems intuitive that serpentinization reactions will tend to be self-limiting; however, hydrothermal systems hosted in extensively serpentinized

ultramafic rocks remain active for thousands of years [e.g., *Früh-Green et al*., 2003]. It is therefore of considerable importance to understand the evolution of permeability in fractured ultramafic rocks.

Previous experimental studies of fault-rock behavior under hydrothermal conditions did not always include permeability measurements [e.g., *Karner et al.*, 1997; *Nakatani*, 1998]. *Moore et al.* [1994] measured the matrix permeability of Westerly granite in the temperature range 300-500˚C at 50 MPa effective pressure, simulating temperature conditions near the base of the seismogenic zone. They found that reduction in permeability and healing and sealing of microfractures resulted from introduction of hydrothermal fluids to heated granite samples. *Evans et al*. [1997] studied the permeability of fault rocks in the damage zone, the undeformed host rock, and the fault gouge, and they concluded that fluid-rock reactions strongly affect the permeability structure of fault zones. *Olsen et al*. [1998] observed permeability cycling during deformation experiments at elevated temperatures resulting from the formation and breaking of mineral seals. *Tenthorey et al*. [1998] and *Aharonov et al*. [1998] related permeability decreases to authigenic mineral formation during diagenesis experiments at elevated temperatures on labradorite/quartz sand. *Polak et al.* [2003] studied the rate of aperture reduction in a natural fracture of a novaculite as a result of mineral dissolution and precipitation.

There are relatively few studies on the linkage between serpentinization reactions and evolution of permeability in ultramafic rocks. *MacDonald and Fyfe* [1985] performed permeability experiments on partially serpentinized intact peridotites at room temperature and obtained values in the range $l0^{-22}$-10^{-21} m^2 for matrix permeability. *Hirose and Hayman* [2008] estimated the matrix permeability of altered ultramafic rocks and serpentinized dunite from Hole 1309D from the Integrated Ocean Drilling Program (IODP) at the AM on MAR to range

between 10^{-19}-10^{-17} m^2, suggesting that permeability was related to the presence of fractures. *Godard et al.* [2013] conducted flow-through experiments on a permeable sintered San Carlos olivine aggregate with grain size of 150–300 μm at 190˚C and 19 MPa using seawater as the transporting fluid. Permeability decreased from 0.9 x 10^{-18} to 0.1 x 10^{-18} m^2 as a result of precipitation of proto-serpentine, brucite and Fe-oxides during 23 days of experiment. *Andreani et al.* [2009] investigated changes in permeability of sintered dunite samples with an average grain size of 80 μm, at confining pressure of 13 MPa and temperature of 160˚C, to study the effect of in-situ carbonation. Their experiments showed an increase in permeability at a rate of 0.0034 m^2/s over 8 hours. None of the previous studies explored the evolution of fracture permeability during serpentinization reactions and hence do not represent the relevant fluid transport properties at mid-ocean ridges, where the permeability is controlled by fractures.

To better understand the linkages between hydraulic properties of ultramafic rocks and chemical reactions, we investigated evolution of fracture permeability (k_f) under hydrothermal conditions where the rates of serpentinization reactions are high. High-temperature flow-through experiments were performed on fractured cores of ultramafic rocks to determine an effective permeability (k_e), which represents the permeability of the sample treated as if it were homogeneous. Room-temperature flow-through experiments were performed on intact disks of ultramafic rocks to determine the matrix permeability (k_m). Estimates of k_m and k_e allowed us to estimate k_f. The samples used in the experiments, described in section 2, were chosen to have different mineral assemblages and textures, to assess the role of lithology on evolution of fracture permeability. Section 3 provides details of the experimental setup. The results, presented in section 4, complement experiments on powdered and sintered samples in which the contact area between fluid and rock is large [e.g. *Godard et al.*, 2013; *Malvoisin et al*., 2012]. Section 5

discusses the rates and possible mechanisms of reduction in fracture permeability and how this study helps us understand the larger permeability structure of fault zones at hydrothermal conditions. Hydrothermal circulation in ultramafic rocks encountered in some areas of oceanic crust may exhibit short-term temporal variations, reflecting the interplay between fracture sealing and fresh fracture generation that contributes to the long life of these systems.

2. Samples and Sample Preparation

2.1. Description of Samples

We used five different ultramafic rocks for these experiments (Table 1). Three, denoted by the symbols TS, JC, and ND respectively, are dunites from the Twin Sisters Range in Washington, Jackson County in North Carolina (NC), and NewDale from the Blue Ridge province in NC, respectively. They contain approximately 85% Mg-rich olivine, less than 10% serpentine and a number of minor components. One sample (SQ) is a harzburgite from near San Quintin, Baja, Mexico, with 80% Mg-rich olivine and 15% orthopyroxene, the remainder being minor minerals. The final sample (BC) is a pyroxenite from the Bushveld Complex, South Africa, containing more than 85% Mg-rich orthopyroxene, less than 10% serpentine, and other minor phases. Grain sizes of the TS and ND samples range between 0.1 mm and 5 mm, whereas the JC, SQ and BC samples are more homogeneous and fine-grained, with grain sizes between 0.05 and 0.2 mm. All of the samples have been partially serpentinized, ranging between 5-8% for ND to less than 1% for SQ. The samples selected for study do not show evidence of surficial weathering.

This suite of rock samples provides a good representation of the ultramafic rock types in the upper mantle [*Bodinier and Godard*, 2004]. Thus, these experiments can be related to serpentinization processes in many geologic settings, such as the forearc mantle [*Hyndman and Peacock*, 2003] and the oceanic crust [*Christensen and Salisbury* 1975].

2.2. Sample Preparation

All samples were cored from hand-sized specimens to form cylinders with nominal diameter of 1.8 cm. After coring, samples were cut to length and end surfaces and circumferences were ground and hand-polished to assure no leakage of pore fluid between the sample and outer silver jacket, as described in section 3.1. Fractured samples used in high temperature experiments were prepared by splitting solid cylinders between steel wedges in an arbor press. These tensile fractures, split parallel to the sample axes, had well mated but rough surfaces that provided more surface area for chemical reactions than if samples had been prepared by saw cutting. Fractured samples had lengths of 2.3 to 2.4 cm. Samples used for estimating matrix permeability were 0.9 to 1.3 cm in length.

3. Experimental Setup and Procedures

We performed experiments on fractured samples of ultramafic rocks using a flow-through, high-pressure, high-temperature triaxial machine. Results of the experiments are expressed in terms of k_e. Then, by assuming a parallel plate model for flow in a tensile fracture and

independently measuring k_m, we calculated time-dependent changes in average fracture aperture b and k_f.

3.1. Fractured Samples

Sample assembly was similar to that in *Morrow et al.* [2014] (Figure 1a). De-ionized water was used as the pore fluid, to minimize corrosion of the plumbing system [*Morrow et al*., 2001]. In order to reduce the degree of disequilibrium between the pore fluid and the fracture walls, a 7.5 mm thick layer of crushed ultramafic rock of the same composition as the cylindrical sample and with a grain size between 0.18 and 1.0 mm was placed upstream of the cylindrical core and within the hot zone of the furnace. Both sides of this porous layer were held in place by stainless steel screen meshes (Figure 1a). Interaction of the pore fluid with the ultramafic rock fragments in the porous layer (Figure 1b) would make the fluid chemistry more realistic for a natural system when it entered the fractured rock core (see also *Morrow et al.* [2001]). This layer is estimated to have ~30% porosity, and it provides negligible resistance to flow (Figure 1b).

The fractured sample (D=1.8-1.9 cm, L=2.3-2.4 cm) and porous layer were placed in a 0.50 mm-thick teflon sleeve between carbide spacers. The whole sample assembly was housed in a 0.38 mm-walled, annealed silver jacket that isolated it from the confining medium and was surrounded by a resistance furnace situated inside the pressure vessel. The upper end of the sample (Figure 1c) was connected to an external pore pressure pump and also housed a thermocouple that measured sample temperature. The lower end of the sample was connected to a second pore-pressure pump and a pore-fluid sampling system (Figure 1c), that was designed to extract fluid that had passed through the sample without reducing pore pressure in the sample.

This is an important element of the experimental design, because the pore water in the sample is in a liquid state and a drop in pore pressure would cause it to flash to steam within the fracture. The experiments were performed at constant confining pressure (P_c) of 50 MPa and pore pressure (P_p) of 20 MPa, yielding an effective pressure (P_e=P_c-P_p) of 30 MPa, simulating a depth of 2 km under hydrostatic fluid pressure conditions. Where possible, a pore pressure difference of 2 MPa was imposed between the top and bottom pore pressure generators, producing a steady-state flow regime.

3.2. Intact Samples

We performed a separate set of room-temperature experiments on intact core samples (D=1.8-1.9 cm, L=0.9-1.3 cm) to determine matrix permeability (k_m). The methodology of the intact experiments is the same as described by *Morrow et al.* [2014], except that we use de-ionized water as pore fluid. Porous Berea sandstone wafers (19 mm diameter by 0.65 mm thickness) with high permeability (>10^{-15} m^2) were placed on the top and bottom of the samples, to provide a uniform pore pressure to the upstream and downstream sample faces. Because the matrix permeability of Berea sandstone is many orders of magnitude higher than that of intact ultramafic rocks, it can be neglected in calculations of permeability from measured flow rates using Darcy's Law. The sample assembly was placed in a latex jacket and secured to steel end plugs.

Flow rate was measured under steady flow conditions at effective pressure (P_e) of 30 MPa and a constant pore-pressure difference of 4 MPa across the sample. The matrix permeability was used in conjunction with k_e to estimate k_f and its evolution as a function of time.

3.3. Experimental Procedures

In each experiment, the sample assembly was first placed in the pressure vessel (Figure 1c) and evacuated to ensure that no air was trapped in the sample or tubing. We then applied confining and pore pressure and measured the permeability at room temperature. In the experiments on fractured samples, the final step was to heat the sample to 260 °C, which is near the temperature for peak reaction rate for serpentinization reactions [*Martin and Fyfe*, 1970]. The heating process lasted 15-20 minutes.

At the beginning of the experiments on fractured samples, permeability was too high for the pore pressure pump to develop a 2 MPa gradient. These samples remained under confining and pore pressure with no flow for 8 to 16 hours between permeability tests. Then pumps were run at maximum flow rate and the pore pressure drop across the sample was measured to determine permeability. Given the maximum flow rate of the pump, the sample dimensions and the sensitivity of the pressure transducers, the maximum permeability that can be measured at 260˚C using Darcy's Law (section 4.1) is approximately 2.6×10^{-16} m^2. Because water has a higher viscosity at room temperature, the upper measurement limit of permeability at room temperature is about 2×10^{-15} m^2.

To measure permeability, valve 2 and valve 3 were closed and valve 1 was open (Figure 1c), so that the pressure difference between the high- and low-side pumps caused pore fluid to flow through the sample. This fluid was stored in the left side of the separator that has a free-moving internal shuttle with O-ring seals. To discharge a fluid sample, valve 1 was closed, valve 3 was opened and the low-side pump was advanced to eject fluid stored in the separator (Figure 1c).

Then the low side was brought back up to operating pressure with the hand pump, resulting in system recharge. The final fluid sample (~0.9 cm^3, comprising 3 full pump strokes) was diluted with 1% nitric acid to a total volume of 3 cm^3 and was analyzed for major cations (Mg, Fe) and silica using an Inductively Coupled Plasma Atomic Emission Spectrometer (ICP-AES).

Polished thin sections of the cross section of the porous layer and sections perpendicular to the fracture in the rock core were prepared after each experiment. Mineral chemistry of the reactants and precipitates was determined using a 5 nA beam current and 1 μm spot size on a Cameca SX50 Electron Microprobe (EMP) equipped with 4 WDS spectrometers. A Camscan Series II Scanning Electron Microscope (SEM) equipped with an upgraded image capture system and an American Nuclear Systems EDS detector was used for high magnification examination of the samples.

4. Results

4.1. Effective Permeability of Fractured Samples

We calculated effective permeability (k_e), assuming Darcy's Law:

$$\frac{Q}{A} = -\frac{k_e}{\eta}\frac{\Delta P}{L} \quad (1)$$

where Q is the volumetric flow rate m^3/s, A is the cross-sectional area of the cylinder m^2, η is the dynamic viscosity of the fluid Pa.s, L is the sample length (m) and ΔP is the applied pore-pressure difference across the sample MPa. In equation (1) k_e denotes the permeability measured as though the flow occurs uniformly through the cross-sectional area A of the cylindrical sample.

Evolution of k_e during the high-temperature experiments is shown in Figure (2). The time t=0 is the time at which the sample reached 260˚C. All of the samples showed at least 2 orders of magnitude drop in effective permeability in the 200-330 hours of the experiments. The initial high temperature values of k_e ranged from 10^{-18} to more than 10^{-16} m^2 and were somewhat variable, because starting permeability was sensitive to how well the two sample halves were mated [*Morrow et al*., 2001]. The initial permeability of samples TS and SQ at 260˚C exceeded the maximum measurable value for the experimental system but decreased into the measurable range after about 50 hours. The final value of k_e ranged between 10^{-18} and 10^{-20} m^2, which is similar to the estimated permeabilities of partially serpentinized peridotites [*MacDonald and Fyfe*, 1985; *Hirose and Hayman*, 2008; *Godard et al.*, 2013, *Tenthorey et al.*, 2003].

Factors contributing to uncertainty in determining k_e include the sample dimensions that appear in equation (1) as the ratio L/A and typically contribute less than 0.5% uncertainty. Pore pressure precision is 0.005 MPa and for a 2 MPa pressure drop across the sample contributes 0.25% uncertainty to the permeability determination. For sample permeability above about 10^{-17} m^2, the pore-pressure generator cannot maintain the desired 2 MPa pressure gradient. For permeability below about 10^{-17} m^2, measurement of flow rate Q dominates the uncertainty in determining permeability. For the range $10^{-20} < k < 10^{-17}$ m^2, uncertainty in Q and therefore k is less than ±5%. For $k < 10^{-20}$ m^2, individual flow tests may take many hours to days and room temperature fluctuations degrade the flow rate determination so that uncertainty in k can increase to ±10% [*Morrow et al.*, 2014].

4.2. Permeability of Intact Samples

Permeability of a set of intact samples was determined using equation (1) where k is now matrix permeability, k_m. All tests were performed at 23˚C and effective confining pressure of 30 MPa. Table 2 shows the estimated values of k_m. The SQ sample contained a preexisting fracture that made permeability measurements unrepresentative of matrix properties.

4.3. Evolution of Fracture Permeability

The effective permeability of the cylindrical samples with a through-going fracture can be treated in terms of layers of different permeability parallel to the flow direction (Figure 1a). Then k_e of the sample calculated from equation (1) can be written as:

$$k_e = \frac{k_m A_m + k_f A_f}{A_m + A_f} \quad (2)$$

where k_f is fracture permeability, $A_f = 2rb$ m^2 is the fracture cross sectional area where r is the radius of the sample and b is the average fracture aperture m, and the total sample cross-sectional area is $A_m + A_f = \pi r^2$ m^2.

Although the fractures generated in the core samples may exhibit significant aperture variations and tortuosity along the flow path, we assume that k_f can be approximated using the cubic law for flow in a fracture represented by parallel plates [*Bear*, 1972; *Witherspoon et al.*, 1980]:

$$k_f = \frac{b^2}{12} \quad (3)$$

By incorporating equation (3) into equation (2):

$$k_e = \frac{k_m(\pi r^2 - 2rb) + \frac{b^2}{12}(2rb)}{\pi r^2} \quad (4)$$

The estimated average fracture aperture, *b*, at the beginning and end of the heated tests was calculated using equation (4) and the measured values of k_e and k_m (Table 2). *b* for all the samples ranges from 0.01 to 1 μm (Table 2) and over the course of each high temperature experiment, it decreases by as much as an order of magnitude.

To investigate evolution of fracture permeability, we substitute the calculated values of *b* into equation (3) to determine k_f both at room temperature and as a function of time at 260˚C (Table 2). Compared with the evolution of k_e in Figure 2, k_f follows the same trend but is approximately 3-6 orders of magnitude greater than k_e and approximately 9 orders of magnitude higher than k_m. These differences indicate that fluid flow in the matrix is negligible and equation (4) can be simplified to:

$$k_e \cong \frac{b^3}{6\pi r} = \frac{2bk_f}{\pi r} \quad (5)$$

Equations (3) and (5) show that for individual experiments, $b \propto {k_e}^{1/3}$ and consequently $k_f \propto {k_e}^{2/3}$. For the SQ sample, we were unable to determine k_m by direct measurement. In this case, we used equation (5) to determine k_f (Figure 4) and *b* (Table 2).

Note that in equations (2) and (4) we use the measured room-temperature value of k_m at P = 30 MPa, even though its value at 260˚C may vary as a result of thermal cracking or mineral

deformation [e.g. *Moore et al.*, 1994]. Calculated k_f is so much greater than k_m that, even though the fracture accounts for less than 0.02% of the cross-sectional area of sample, flow in the fracture still dominates flow in the rock matrix. Reynolds number for flow focused in a fracture can be estimated using $Re = \rho v b/\eta$ where ρ is density of (10^3 kg/m^3), $v=Q/A$ is velocity of pore fluid in the fracture ($A=bd$) that ranges between $3x10^{-3}$-$2x10^{-2}$ (m/s) and η is the viscosity of water at 260˚C (0.000096 Pa.s). *Re* values fall in the range 10^{-3}-10^{-1}, which indicates laminar flow in the fracture.

4.4. Rock Mineralogy and Fluid Chemistry data

The Back-Scattered Electron (BSE) images collected using SEM (Figure 4) show needle-shaped crystals precipitated along the walls of the fracture and on the surfaces of loose grains that may have moved along the fracture during flow [more images available in *Farough*, 2015]. In all of the samples, more than 50% of the length of the tensile fracture has new precipitation (Figure 4a,b) and about 10% of the fracture length is blocked with loose grains (Figure 4c).

The EMP analyses revealed that alteration products are mainly rich in SiO_2, MgO, and FeO , and the compositions are consistent with the mineral serpentine (Table 3). The Mg/(Mg+Fe) ratio of the newly precipitated serpentine in all peridotite samples is 0.9. The concentrations of SiO_2 and MgO of precipitates in the TS, JC and ND dunite samples are higher than those in the SQ sample. The FeO contents of the serpentine deposits in all peridotite samples are less than 10 wt%, and the concentrations of Al_2O_3, TiO_2, Cr_2O_3 and CaO are less than ~3 wt%. The high Fe contents of the serpentine from the BC pyroxenite may indicate precipitation of serpentine accompanied by an Fe-rich phase. Most of the new precipitates in all of the samples lined the

wall of the tensile fracture; negligible amounts of precipitated material were detected in the intergranular pores of the layers of crushed rock above the samples. There is no evidence of brucite precipitation in any of the samples. A similar result has been observed before by *Okamoto et al.* [2011], where continuous supply of fresh fluid causes the serpentinization reactions to proceed without the formation of brucite. *Klein et al.* [2015] also did not observe brucite in their experiments, as a result of simultaneous dissolution of olivine and orthopyroxene.

The ideal case for fluid sampling and analysis would be that a 2 MPa pore-pressure gradient is maintained across the sample cell, allowing for slow, continuous flow. However, as described previously (section 3.3), at the beginning of experiments the 2 MPa pore-pressure gradient was not reached. The total fluid volume contained in the porous layer (assuming ~30% porosity) plus the fracture (assuming the average estimated aperture from Table 2) was calculated to be $\leq$0.6 cm^3. Given that the volume of each fluid sample collected is ~0.9 cm^3, the first fluid samples contain a considerable proportion of essentially unreacted deionized water that was rapidly flushed through the system. As permeability and flow rates decrease, the amount of time required for an increment of fluid to traverse the fracture increases. The final fluid sample collected during an experiment therefore comes closest to equilibration with the rock sample. Concentrations of Mg, Fe, Si, Na, Ca, Al increased from zero in de-ionized water to 10^{-5}-10^{-3} molar in the final pore fluid sample. The overall trend of fluid chemistry exhibits significant increases in the key chemical constituents of serpentinization reactions that are consistent with dissolution of ultramafic rocks at high temperature. The fluid chemistry data is only used as evidence that water-rock reactions occurred and more detailed analysis of fluid chemistry is out of the scope of this paper.

5. Discussion

5.1. Rate of Reduction of Fracture Permeability with Time

The reduction in fracture permeability with time fits an exponential function:

$$k_f = k_{f0} e^{(-\frac{t}{t^*})} \quad (6)$$

where k_{f0} is the starting permeability of the modeled interval and t* is the characteristic decay time of the best fit exponential function in hours. Figure 3 shows the results. In order to obtain a better fit, the last one or two data points, which depict a rapid decrease in permeability at the end of TS, SQ, BC and ND experiments (see Figure 2), were removed. These points most probably refer to other physical processes that started later in the experiments. The decay time of fracture permeability varies by approximately a factor of 3, ranging between approximately 50 and 143 hours (Table 4). There is no apparent relationship between lithology and measured decay time for the experiments.

Previous laboratory studies on the evolution of permeability in both intact and fractured granitic rocks [*Moore et al*., 1994; *Morrow et al*., 2001] also showed that the rate of permeability decrease fits an exponential function after a rapid initial decline in permeability. The experiments of *Morrow et al.* [2001] on fractured samples of granite at 150 and 250˚C at 150 MPa confining pressure and 100 MPa pore pressure exhibited decay times between approximately 730 and 1580 hours. Notably, the decay times for the ultramafic rocks are all significantly shorter than for the granitic rocks under generally similar *P*-*T* conditions. The difference in decay times for

ultramafic and granitic rocks suggests that the rate of reaction in ultramafic rocks is faster than that in granitic rocks under these experimental conditions.

5.2. Mechanisms of Reduction in Fracture Permeability

The changes in permeability and aperture of a natural, rough-walled fracture during flow under hydrothermal conditions can be affected by a number of factors. The most important and effective among these are mineral dissolution and precipitation along the walls of the fracture, pressure solution of contacting asperities, transport of fine-grained solids along the flow path and thermal cracking and fracture morphology. Mineral dissolution at free faces of the fracture and thermal cracking act to increase permeability, whereas mineral precipitation and pressure solution of contacting asperities act to decrease permeability. Transport of fine grains and tortuosity of the flow path can affect permeability in various ways. For example, blockage of the flow path with loose mineral grains (Figure 4c) acts to reduce permeability and increase tortuosity, whereas dissolution or breakage of the blocked grains has the opposite effect.

The SEM images (Figure 4a, b, c) show that mineral precipitation and blockage of the flow path with loose grains did take place. A comparison between estimated average aperture, *b*, in Table 2 with observed aperture in Figure 4a, b, c (~2 to 6 μm) suggests that the spatial arrangement of the aperture distribution is strongly heterogeneous. The equal height of the precipitates in Figure 4a and b suggests that the width of the fracture was spanned with precipitates, and that after the confining pressure was removed and/or during sectioning of the samples, the fracture reopened.

The parallel plate law, used in estimating average aperture, assumes that the tortuosity of the flow path is negligible and that fracture roughness can be described as though all the flow is parallel to the pressure gradient [e.g., *Tsang*, 1984]. But in reality, in a rough-walled fracture under confining pressure, portions of the fracture may be closed as a result of mineral dissolution and precipitation reactions, leading to a reduction in fracture aperture and an increase in tortuosity of the flow path. As the tortuosity increases, the effective fracture permeability may be significantly smaller than given by the cubic law [*Tsang*, 1984]. Detailed analysis of the changes in topography of the fracture walls and the aperture widths over time is required to investigate the effect of tortuosity on the evolution of fracture permeability. Techniques such as surface profilometery [e.g. *Durham et al.*, 2001; *Ameli et al.*, 2013] and X-ray Computed Tomography (CT) imaging [e.g. *Polak et al.*, 2004] can help to better understand the spatial configuration of the fracture surface.

5.3. Implications for Mid-Ocean Ridge Hydrothermal Systems

The goal of this study was to better understand the processes controlling hydraulic properties of the host rock during serpentinization reactions in ultramafic-hosted hydrothermal systems in oceanic crust, given that flow is primarily controlled by fractures. We understand the limitations of applying a 2 week long study of a single fracture with an aperture on the scale of microns to a complicated network of natural fractures encompassing a range of sizes that were subjected to tens to hundreds of years of fluid circulation. Nevertheless, extrapolating our results (Figure 3) to longer times suggests that the permeability of a fracture ~10^{-6} m in width would decay to k_f ~10^{-23} m^2 in approximately 2-4 months, rendering the fracture effectively impermeable. Hence,

mechanisms to open new surface area to fluid flow must occur to maintain the hydrothermal circulation in ultramafic rocks in seafloor hydrothermal systems. Factors such as tectonic activity [*Andreani et al*., 2009] and crystallization pressure [e.g., *Andreani et al.*, 2007; *Kelemen and Hirth*, 2012] coupled with mineral precipitation may result in cyclic behavior of fluid circulation in different regions of oceanic crust, with impermeable mineral seals in one region and high permeability levels in a neighboring region.

Although permeability decreased rapidly as a function of time in these experiments, figure 4c shows short, thin fractures that could have extended away from etch pits. If experiments were run for greater durations, these small fractures might eventually contribute to a secondary fracture network, thereby generating new permeability [e.g., *Malvoisin et al., 2012*; *Kelemen and Hirth*, 2012]. Some analyses of mineralized fractures in IODP samples indicate different generations of fractures in fracture networks [*Beard et al.*, 2009].

Fluid circulation in seafloor hydrothermal systems is fed by a large system of fractures that are continually plugging and fracturing in different places. These processes likely create a heterogeneous permeability structure in oceanic crust, which could affect the behavior or the life cycle of seafloor hydrothermal systems.

6. Conclusions

This study monitors changes in permeability of fractured samples of ultramafic rocks under hydrothermal conditions, in order to better understand the rate at which serpentinization reactions affect fracture permeability and to shed some light on the linkages between the physical and chemical changes of the oceanic crust during hydrothermal circulation in ultramafic rocks.

For a variety of rock lithologies, the experimental results show that fracture permeability decreased as much as two orders of magnitude during the 200-330 hours of the high temperature experiments.

Although a number of factors may have contributed to the decrease in permeability, precipitation of serpentine minerals along the walls of the tensile fracture played an important role. These results suggest that serpentinization reactions can block flow paths and impede fluid circulation in the oceanic crust in a relatively short time, even with the limited reactive surface area available in fractures. Long-term maintenance of fluid circulation in ultramafic-hosted hydrothermal systems requires frequent generation of new permeable pathways, perhaps by a combination of tectonic activity and crystallization pressure.

Acknowledgments

The authors thank Neil Johnson for XRD assistance and sample collection, Luca Fedele for EMP and SEM assistance. Edmond A. Mathez and the American Museum of Natural History, NY provided some of the samples. Lee-Grey Boze helped with the sample preparation and collection of intact permeability data. C. Neuzil and J. Taron provided constructive reviews of an early draft of the paper. The authors also would like to thank J. Donald Rimstidt, James Beard and Esther Schwarzenbach, for useful conversations regarding serpentinization processes and data interpretation. This work was partially supported by NSF grant OCE1131471 to RPL. All data used in this paper can be found in the tables and has been properly cited. . The raw experimental data is available upon request.

7. References

Aharonov, E., E. Tenthorey, and C. H. Scholz (1998), Precipitation sealing and diagenesis: 2. Theoretical analysis, *Journal of Geophysical Research*, *103*(B10), 23969.

Ameli, P., J. E. Elkhoury, and R. L. Detwiler (2013), High-resolution fracture aperture mapping using optical profilometry, *Water Resources Research*, *49*(10), 7126-7132.

Andreani, M., C. Mével, A. M. Boullier, and J. Escartín (2007), Dynamic control on serpentine crystallization in veins: Constraints on hydration processes in oceanic peridotites, *Geochemistry Geophysics Geosystems*, *8*, Q02012, doi:10.1029/2006GC001373.

Andreani, M., L. Luquot, P. Gouze, M. Godard, E. Hoise, and B. Gibert (2009), Experimental study of carbon sequestration reactions controlled by the percolation of CO_2-rich brine through peridotites, *Environmental Science & Technology*, *43*(4), 1226-1231.

Bach, W., N. R. Banerjee, H. J. Dick, and E. T. Baker (2002), Discovery of ancient and active hydrothermal systems along the ultra-slow spreading Southwest Indian Ridge 10°–16°E, *Geochemistry Geophysics Geosystems*, *3*(7), 1-14.

Batuyev, B. N., A. G. Krotov, V. F. Markov, G. A. Cherkashev, S. G. Krasnov, and Y. D. Lisitsyn (1994), Massive sulfide deposits discovered and sampled at 14°45′N, Mid-Atlantic Ridge, *BRIDGE Newsletter*, *6*, 6–10.

Bear, J. (1972) Dynamics of Fluids in Porous Media, *Elsevier*, New York.

Beard, J. S., B. R. Frost, P. Fryer, A. McCaig, R. Searle, B. Ildefonse, P. Zinin, and S. K. Sharma (2009), Onset and Progression of Serpentinization and Magnetite Formation in Olivine-rich Troctolite from IODP Hole U1309D, *Journal of Petrology*, *50*(3), 387-403.

Bogdanov, Y. A., A. M. Sagalevitch, E. S. Chernyaev, A. M. Ashadze, E. G. Gurvich, V. N. Lukashin, G. V. Ivanov, and V. N. Peresypkin (1995), A study of the hydrothermal field at

14°45′N on the Mid-Atlantic Ridge using the “Mir” submersibles, *BRIDGE Newsletter*, *9*, 9–13.

Bodinier, J., and M. Godard (2004), Treatise on Geochemistry, Volume 2: The Mantle and Core.

Cann, J., D. Blackman, D. Smith, E. McAllister, B. Janssen, S. Mello, E. Avgerinos, A. Pascoe, and J. Escartin (1997), Corrugated slip surfaces formed at ridge-transform intersections on the Mid-Atlantic Ridge, *Nature*, *385*(6614), 329-332.

Cannat, M. (1993), Emplacement of mantle rocks in the seafloor at mid-ocean ridges, *Journal of Geophysical Research: 98*(B3), 4163-4172.

Carlson, R. (2001), The abundance of ultramafic rocks in Atlantic Ocean crust, *Geophysical Journal International*, *144*(1), 37-48.

Christensen, N. I., and M. H. Salisbury (1975), Structure and constitution of the lower oceanic crust, *Reviews of Geophysics*, *13*(1), 57-86.

Coleman, R. G. (1971), Petrologic and geophysical nature of serpentinites, *Geological Society of America Bulletin*, *82*(4), 897-918.

Connelly, D. P., J. T. Copley, B. J. Murton, K. Stansfield, P. A. Tyler, C. R. German, and S. Wilcox (2012), Hydrothermal vent fields and chemosynthetic biota on the world's deepest seafloor spreading centre, *Nature communications*, *3*, 620, doi:10.1038/ncomms1636.

Durham, W. B., W. L. Bourcier, and E. A. Burton (2001), Direct observation of reactive flow in a single fracture, *Water Resources Research*, *37*(1), 1-12.

Escartin, J., G. Hirth, and B. Evans (2001), Strength of slightly serpentinized peridotites: Implications for the tectonics of oceanic lithosphere, *Geology*, *29*(11), 1023-102.

Evans, J. P., C. B. Forster, and J. V. Goddard (1997), Permeability of fault-related rocks, and implications for hydraulic structure of fault zones, *Journal of Structural Geology*, *19*(11),

1393-1404.

Farough, A. (2015), An experimental study on characterization of physical properties of ultramafic rocks and controls on evolution of fracture permeability during serpentinization at hydrothermal conditions, *Ph.D. Thesis*, Virginia Tech, Blacksburg, VA.

Früh-Green, G. L., D. S. Kelley, S. M. Bernasconi, J. A. Karson, K. A. Ludwig, D. A. Butterfield, C. Boschi, and G. Proskurowski (2003), 30,000 years of hydrothermal activity at the Lost City vent field, *Science*, *301*(5632), 495-498.

Godard, M., L. Luquot, M. Andreani, and P. Gouze (2013), Incipient hydration of mantle lithosphere at ridges: A reactive-percolation experiment, *Earth and Planetary Science Letters*, *371*, 92-102.

Hirose, T., and N. Hayman (2008), Structure, permeability, and strength of a fault zone in the footwall of an oceanic core complex, the Central Dome of the Atlantis Massif, Mid-Atlantic Ridge, 30°N, *Journal of Structural Geology*, *30*, 1060-1071.

Hyndman, R. D., and S. M. Peacock (2003), Serpentinization of the forearc mantle, *Earth and Planetary Science Letters*, *212*(3-4), 417-432.

Karner, S. L., C. Marone, and B. Evans (1997), Laboratory study of fault healing and lithification in simulated fault gouge under hydrothermal conditions, *Tectonophysics*, 277, 41-55.

Kelemen, P. B., and G. Hirth (2012), Reaction-driven cracking during retrograde metamorphism: Olivine hydration and carbonation, *Earth and Planetary Science Letters*, *345*, 81-89.

Kelley, D. S., J. A. Karson, D. K. Blackman, G. L. Früh-Green, D. A. Butterfield, M. D. Lilley, and P. Rivizzigno (2001), An off-axis hydrothermal vent field near the Mid-Atlantic Ridge at 30 N, *Nature*, *412*(6843), 145-149.

Klein, F., N. G. Grozeva, J. S. Seewald, T. M. McCollom, S. E. Humphris, B. Moskowitz, T. S. Berquo, and W.-A. Kahl (2015), Experimental constraints on fluid-rock reactions during incipient serpentinization of harzburgite, *American Mineralogist*, *100*(4), 991-1002.

Lowell, R. P., A. Farough, J. Hoover, and K. Cummings (2013), Characteristics of magma-driven hydrothermal systems at oceanic spreading centers, *Geochemistry Geophysics Geosystems*, *14*(6), 1756-1770.

Macdonald, A., and W. Fyfe (1985), Rate of serpentinization in seafloor environments, *Tectonophysics*, *116*(1), 123-135.

Malvoisin, B., F. Brunet, J. Carlut, S. Rouméjon, and M. Cannat (2012), Serpentinization of oceanic peridotites: 2. Kinetics and processes of San Carlos olivine hydrothermal alteration, *Journal of Geophysical Research*, *117*, B04102, doi:10.1029/2011JB008842.

Martin, B., and W. Fyfe (1970), Some experimental and theoretical observations on the kinetics of hydration reactions with particular reference to serpentinization, *Chemical Geology*, *6*, 185-202.

Moore, D. E., D. A. Lockner, and J. D. Byerlee (1994), Reduction of permeability in granite at elevated temperatures, *Science*, *265*(5178), 1558-1561.

Morrow, C. A., D. E. Moore, and D. A. Lockner (2001), Permeability reduction in granite under hydrothermal conditions, *Journal of Geophysical Research 106*(B12), 30551-30560.

Morrow, C., D. Lockner, D. Moore, and S. Hickman (2014), Deep permeability of the San Andreas Fault from San Andreas Fault Observatory at Depth (SAFOD) core samples, *Journal of Structural Geology*, *64*, 99-114.

Nakatani, M. (1998), A new mechanism of slip weakening and strength recovery of friction associated with the mechanical consolidation of gouge, *Journal of Geophysical Research, 103*, 27239-27256.

O'Hanley, D. S. (1992), Solution to the volume problem in serpentinization, *Geology*, *20*(8), 705-708.

Okamoto, A., Y. Ogasawara, Y. Ogawa, and N. Tsuchiya (2011), Progress of hydration reactions in olivine–H_2O and orthopyroxenite–H_2O systems at 250˚C and vapor-saturated pressure, *Chemical Geology*, *289*(3–4), 245-255.

Olsen, M. P., C. H. Scholz, and A. Léger (1998), Healing and sealing of a simulated fault gouge under hydrothermal conditions: Implications for fault healing, *Journal of Geophysical Research*, *103*(B4), 7421-7430.

Polak, A., D. Elsworth, H. Yasuhara, A. Grader, and P. Halleck (2003), Permeability reduction of a natural fracture under net dissolution by hydrothermal fluids, *Geophysical Research Letters*, *30*, 2020, doi:10.1029/2003GL017575, 20.

Polak, A., D. Elsworth, J. Liu, and A. S. Grader (2004), Spontaneous switching of permeability changes in a limestone fracture with net dissolution, *Water Resources Research*, *40*, W03502, doi:10.1029/2003WR002717.

Tenthorey, E., C. H. Scholz, E. Aharonov, and A. Léger (1998), Precipitation sealing and diagenesis: 1. Experimental results, *Journal of Geophysical Research*, *103*(B10), 23951-23967.

Tenthorey, E., S. F. Cox, and H. F. Todd (2003), Evolution of strength recovery and permeability during fluid–rock reaction in experimental fault zones, *Earth and Planetary Science Letters*, *206*(1), 161-172.

Tsang, Y. (1984), The effect of tortuosity on fluid flow through a single fracture, *Water Resources Research, 20*(9), 1209-1215.

Witherspoon, P. A., J. S. Y. Yang, K. Iwari and J. E. Gale (1980), Validity of cubic law for fluid flow in a deformable rock fracture, *Water Resources Journal, 16*, 1016-1024.

8. Figures

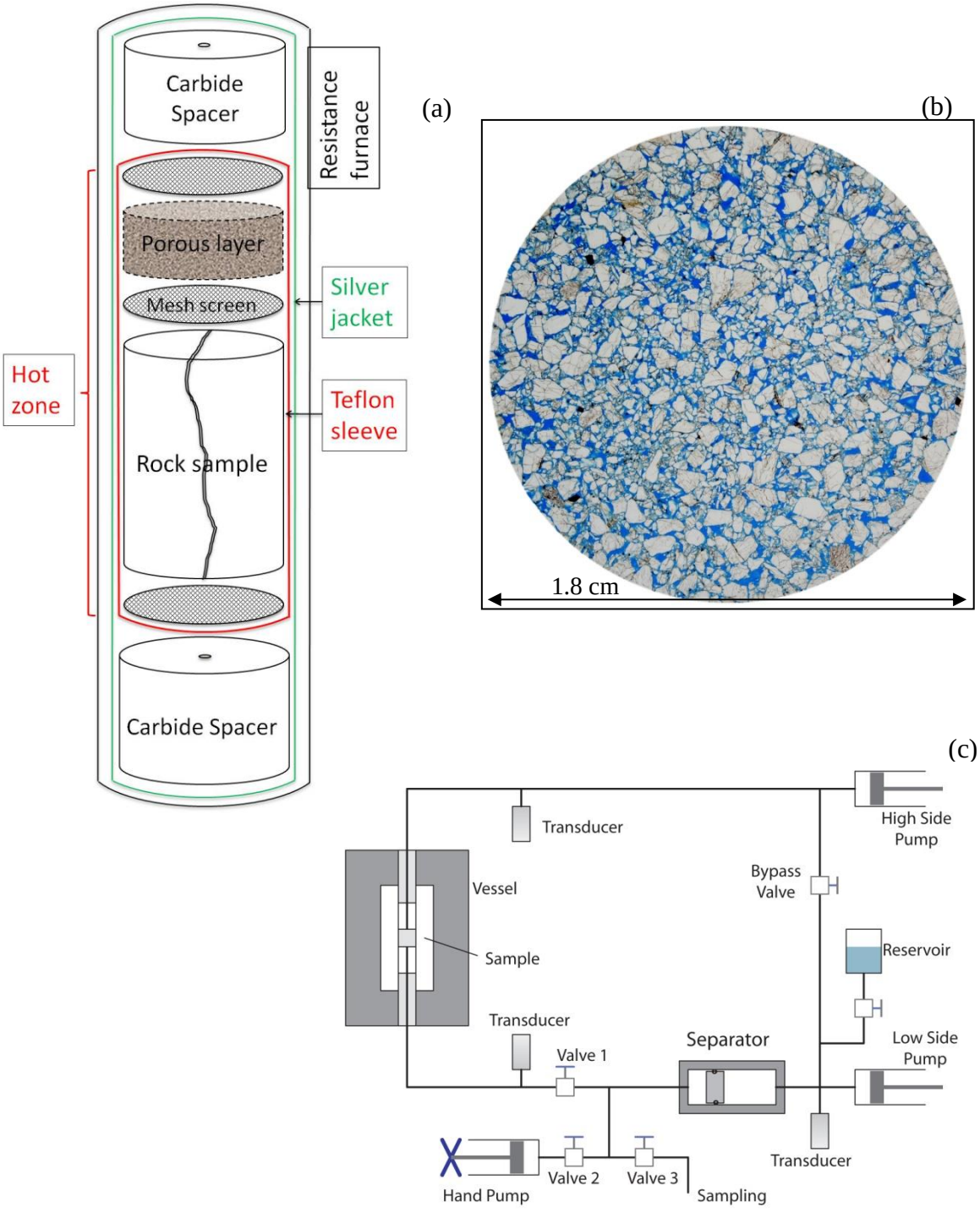
(a)
Carbide Spacer
Resistance furnace
Porous layer
Silver jacket
Mesh screen
Hot zone
Teflon sleeve
Rock sample
Carbide Spacer
(b)
1.8 cm
(c)
Transducer
High Side Pump
Bypass Valve
Vessel
Sample
Reservoir
Transducer
Separator
Low Side Pump
Valve 1
Transducer
Valve 2
Valve 3
Hand Pump
Sampling

Figure (1): (a) The furnace assembly for fractured-sample experiments at elevated temperatures. (b) Cross section of the crushed-rock layer. The pore spaces are filled with blue epoxy; the porosity of the layer in all experiments is ~30%. (c) The set-up of the pore-pressure system. The solute-free fluid is stored in the reservoir. If the bypass valve is open, fresh water is let into the system, and the high-side pump directs the fluid the sample.

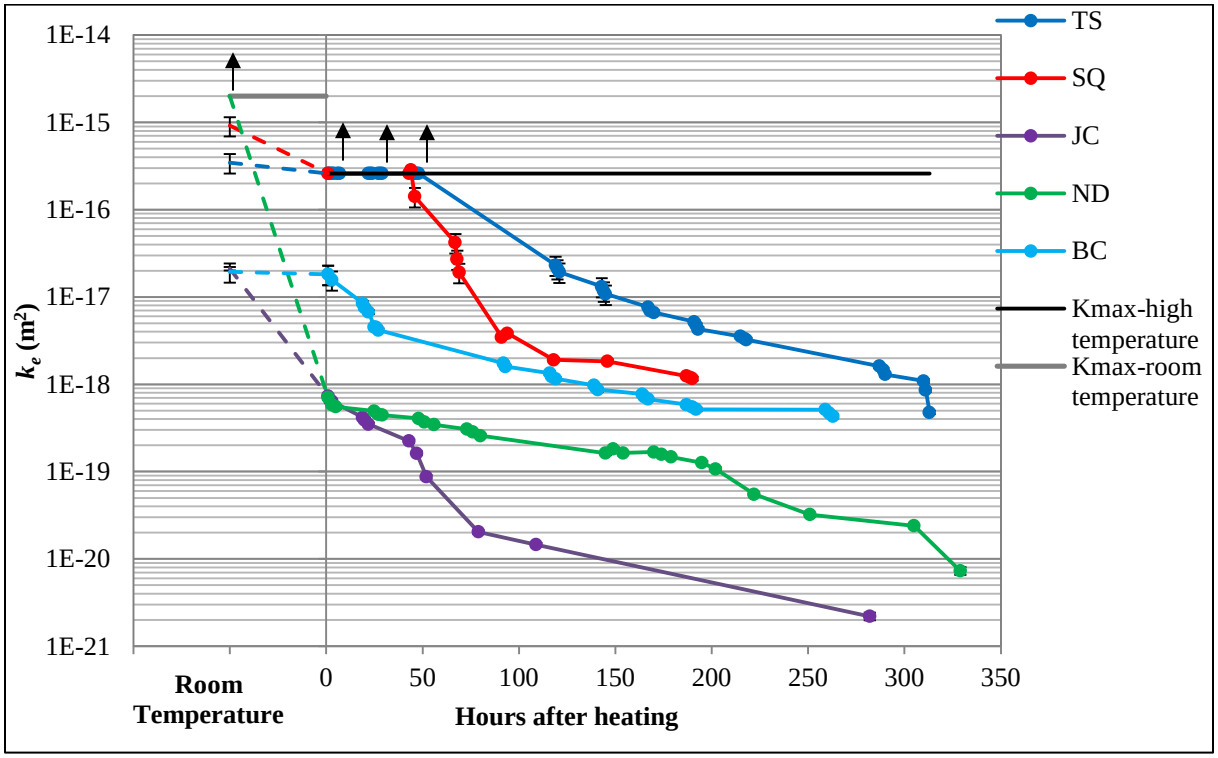

Figure (2): Evolution of effective permeability k_e of the fractured sample, where k_e is calculated assuming that flow is distributed across the cross-sectional area of the cylinders. Time = 0 is when the sample reached 260˚C. Each measurement is averaged over the time it takes for a full stroke of the high side pump, which is 0.3 cc. Gray and black lines represent the maximum measureable permeability at room temperature and 260˚C, respectively. The upward-pointing arrows indicate permeabilities that are at or above the maximum measureable limit.

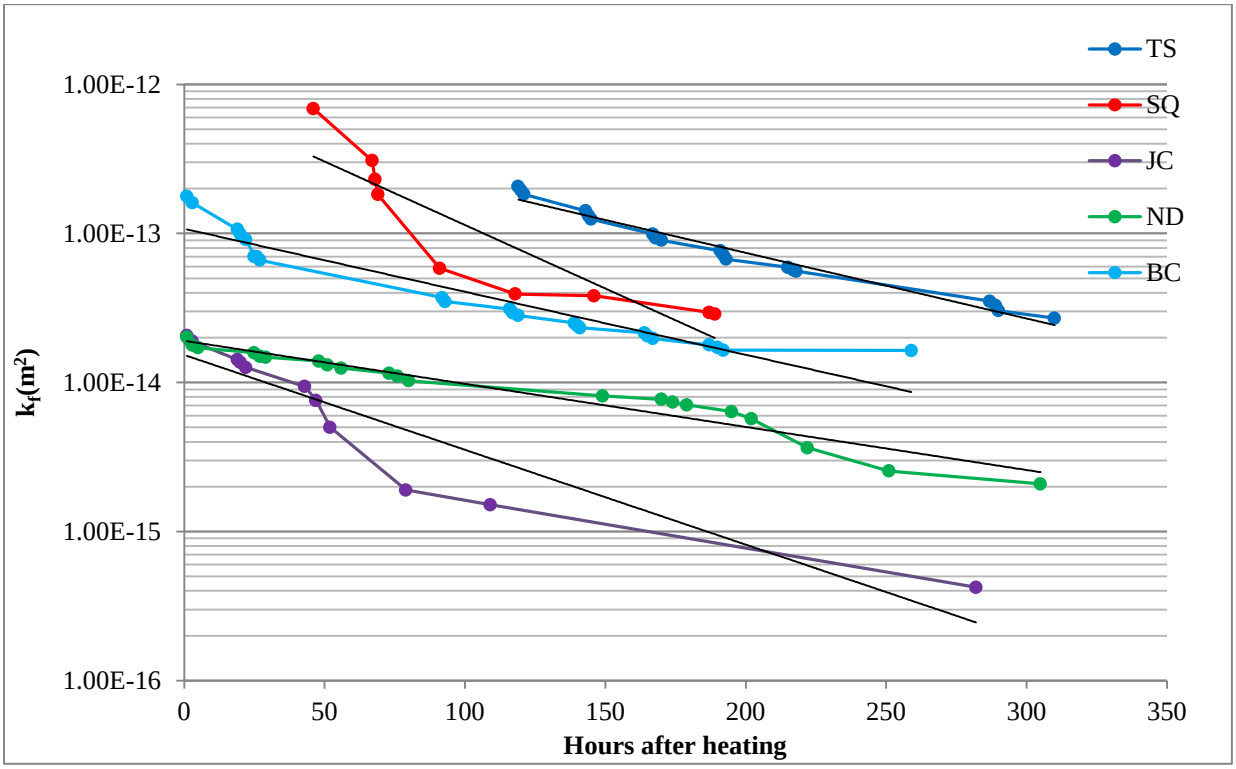

Figure (3): Fitted exponential functions to estimated k_f values presented in Table (2).

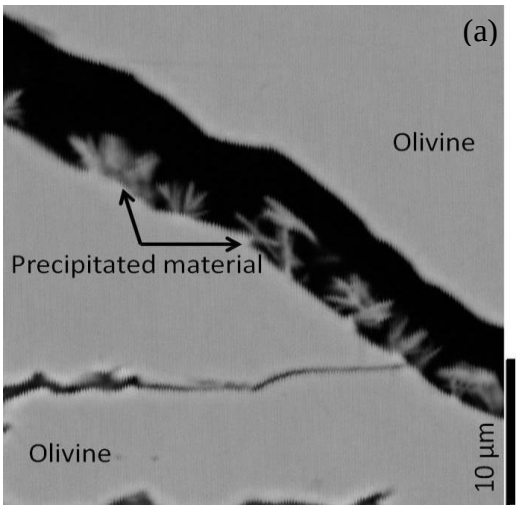

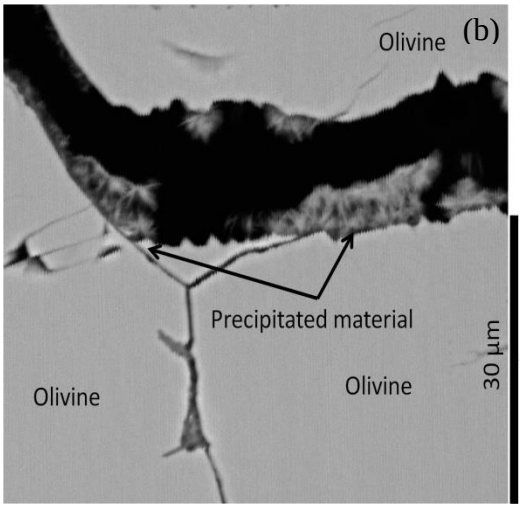

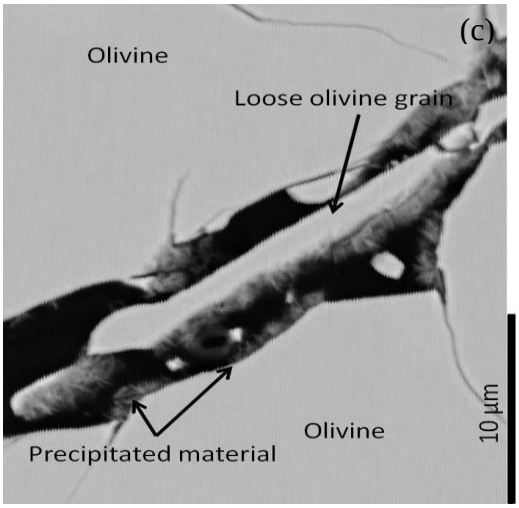

Figure (4): (a-c) BSE images of the tensile fracture and (d) cross-sectional view of the porous layer in the TS sample. (a) and (b) Needle-shaped crystals precipitated along the wall of the fracture. (c) Precipitation of needle-shaped crystals along the walls of the fracture and along the sides of a loose grain.

9. Tables

Table (1): Description of the samples used for the experiments.

Sample		Locality	Average grain size (mm)	Mineral assemblage	
				Major phase (~80-90%)	Other phases (~10-20%)
Dunite	TS	Twin Sisters, WA	0.2-5	Olivine ($Mg_{1.8}$, $Fe_{0.2}$)	Serpentine(1-2%), opx (5-10%), chromium spinel (<2%)
	JC	Jackson County, NC	0.1-0.3	Olivine ($Mg_{1.7}$, $Fe_{0.3}$)	Serpentine(2-4%), talc (<1%), actinolite/tremolite (2-5%), chlorite (<1%), chromium spinel (2-5%),
	ND	Spruce Pine, NC	0.1-0.6	Olivine ($Mg_{1.8}$, $Fe_{0.2}$)	Serpentine(5-8%),Talc (2%), chlorite (2%), actinolite/tremolite (2%)
Harzburgite	SQ	1.5 km southwest of San Quintin, Baja, Mexico	0.05-1	Olivine ($Mg_{1.64}$, $Fe_{0.36}$)	Serpentine(<1%),Opx (15%), chromium spinel (2-5%)
Pyroxenite	BC	east of Bushveld complex, South Africa	0.05-0.2	Orthopyroxene ($Mg_{0.56}$, $Fe_{0.44}$)	Serpentine (2-4%), plagioclase (2-4%), talc (2%), olivine (5%)

* Compositions are provided using XRD, Rigaku's PDXL software (version 1.8)

Table (2):

Estimates of matrix permeability (*km*) at room temperature and fracture permeabilit (*kf*) and aperture (*b*) near the beginning and at the end of the high-temperature experiments.

Sample	23˚C	260˚C		
	k_m (m^2 x 10^{-23})	time (hrs)	k_f* (m^2 x 10^{-16})	b (m x 10^{-6})
TS	3.12	119	2070	1.58
		313	155	0.43
SQ	—	46	6870	2.90
		190	281	0.58
JC	3.14	1	206	0.50
		282	4.2	0.07
ND	20.30	1	201	0.50
		329	9.2	0.10
BC	4.61	1	1770	1.46
		263	146	0.42

* Estimates for TS, JC, ND, and BC are calculated using equation (4) and for SQ using equation (5).

Table (3): The chemical composition of newly precipitated material in the fracture from microprobe analysis.

Sample	TS	SQ	JC	ND	BC
SiO_2	39.76	37.71	41.00	39.12	37.79
MgO	37.05	33.29	39.92	38.59	17.95
FeO	5.97	8.00	3.43	4.34	26.01
Al_2O_3	0.25	1.45	0.06	0.02	2.79
TiO_2	0.02	0.13	0.01	0.00	0.12
Cr_2O_3	0.09	0.05	0.02	0.03	0.13
CaO	0.10	0.71	0.05	0.04	0.63
Total	83.24	81.34	84.48	82.15	85.42
Mg/ (Mg+Fe)	0.92	0.88	0.96	0.94	0.59
Serpentine composition	$(Mg, Fe, Al^{VI}, Ti, Cr, Ca)_6 (Si, Al^{IV})_4 O_{10} (OH)_8$				

Table (4): The slope, ratio of standard error (STD error) to the estimated value and R^2 values of fitted exponential equations to the fracture permeability estimates.

	Time (hours)	k_{f0} (m^2 x 10^{-14})	STD error/estimate	t* (hours)	STD error/estimate	R^2
TS	119-310	60	0.004	100	0.046	0.97
SQ	46-189	80	0.015	50	0.168	0.80
JC	1-282	1	0.005	67	0.122	0.87
ND	1-305	2	0.002	143	0.063	0.94
BC	1-259	9	0.003	100	0.076	0.90

Chapter 3: The Rate of Transformation of Forsterite and Enstatite to Serpentine Determined from an Experimental Study on Evolution of Fracture Permeability in Ultramafic Rocks at Hydrothermal Conditions

Abstract

Serpentinization reactions have a complex nature, in which olivine and pyroxene are replaced by serpentine and other minerals. In this chapter a model that estimates the rate of transformation of olivine to serpentine in a tensile fracture is presented. The model uses the experimental data reported by *Farough et al.*, [2015] on evolution of fracture permeability, using the cubic law, during serpentinization reactions using ultramafic rock cores at temperature of 260˚C and effective pressure of 30 MPa. Assuming the dissolution and precipitation reactions occur simultaneously; the rate of transformation at the beginning of the experiments is ~ 10^{-8}-10^{-9} (mol/m^2 s) and decreases monotonically by about an order of magnitude towards the end of the experiment. I convert the rate of transformation to rate of reaction and the results are similar to estimates of *Martin and Fyfe*, [1970] where they investigated hydration rate of olivine and pyroxene to serpentine-brucite and serpentine-talc at temperatures ranging between 80-560˚C and pressures of 68.94-275.8 MPa for grain size 58-175 μm. The results show that dissolution and precipitation is the main mechanism contributing to the reduction in fracture aperture and that the cubic law is a reasonable approximation for relating changes in aperture as a result of dissolution and precipitation to fracture permeability. The slowing of the transformation rate with increasing time likely occurs because the reactive surface area of reactants decreases with time as precipitates form on the walls of the fracture.

1. Introduction

Serpentinization reaction refers to a set of hydration reactions in ultramafic rocks, in which olivine and pyroxene are replaced by serpentine, magnetite, brucite, talc, and carbonate minerals along with production of dissolved H_2, CH_4 and SiO_2 [e.g., *Abrajano et al.*, 1988; *Barnes et al.*, 1978; *Neal and Stanger*, 1983]. The precise product assemblages in serpentinization reactions depend on temperature, pressure, and bulk composition of the host rock [e.g. *Evans*, 1977*; Manning*, 1995]. Serpentinization reactions alter chemical, mechanical, magnetic, seismic, and hydraulic properties of the host rock [e.g., *Coleman*, 1971; *O'Hanley*, 1992*Miller and Christensen*, 1997; *Carlson*, 2001; *Cannat*, 1993; *Dyment et al.*, 1997] and occur at many geologic settings such as slow and ultra slow mid oceanic ridges [e.g. *Cann et al.*, 1997; *Escartin et al*., 2001; *Smith et al.*, 2008], rifted margins [e.g. *Zonenshain et al.*, 1989; *Reston*, 2009], ocean-continent transition zones [e.g. *Escartin et al*., 2003] and subduction zones [e.g. *Hyndman and Peacock*, 2003; *Skelton and Jakobsson*, 2007; *Faccenda et al.*, 2008; *Hilairet and Reynard*, 2009]. Understanding the extent and rate of serpentinization in the oceanic crust is critical to understanding plate boundary processes, such as volcanism in subduction zones [*Rupke et al.*, 2004] or hydrothermal activity at mid ocean ridges [*Kelly et al.*, 2001] and water cycle and elemental budget of oceans [*Schmidt et al.*, 2007].

Many experimental studies have investigated the interactions between ultramafic rocks and fluids during hydrothermal experiments [e.g. *Allen and Seyfried*, 2003; *Janecky and Seyfried*, 1986; *Seyfried and Dibble*, 1980; *Seyfried et al.*, 2007]. Some studies have focused on the extent and rate of hydration reactions or precipitation of serpentine; others have focused on dissolution rate of olivine and pyroxene. For example, *Martin and Fyfe*, [1970] experimentally investigated

the hydration rate of olivine and pyroxene to serpentine-brucite and serpentine-talc at temperatures ranging between 80-560˚C and pressures of 68.94-275.8 MPa for grain size 58-175 μm. The conversion rates in *Martin and Fyfe*, [1970] were calculated based on the reactant to water weight ratio. *Wegner and Ernst,* [1983] tested the kinetics of olivine to serpentine and brucite reaction using synthetic material at a temperature range of 188-388˚C under pressures of 1-3 Kbar. They concluded that the rate of serpentinization is controlled by the rate of diffusion of water through the grains. *Okamoto et al.*, [2011] conducted experiments in olivine-H_2O and pyroxene-H_2O systems at 250˚C and vapor saturated pressure. They found that the olivine reaction was faster than the pyroxene reaction and progress of hydration reactions depends on evolution of mechanical properties of host rock. *Malvoisin et al.,* [2012] investigated the kinetics of the olivine to serpentine reaction at 50 MPa in the 250-350˚C range using San Carlos Olivine with grain size between 1-150 μm. They conclude that the kinetics of the reaction is inversely proportional to the surface area of the starting olivine grains. But none of the previous studies focused on precipitation induced permeability reduction during serpentinization reactions.

Regarding the dissolution rate of major phases in ultramafic rocks, *Rimstidt et al.,* [2012] systematically reviews data on the dissolution of forsterite, but there is no study at T>150˚C. *Oelkers and Schott,* [2001] provide enstatite dissolution rates at temperatures up to 168˚C. There are no data available on dissolution rate of olivine and pyroxene above 150˚C and 168˚C, respectively.

This paper reports the rates of transformation from olivine and pyroxene to serpentine derived from experiments performed on different samples of ultramafic rocks with a single through going tensile fracture at effective pressure of 30 MPa and temperature of 260°C. This work differs from previous estimates of reaction rate using powdered or sintered samples [e.g.

Martin and Fyfe, 1970; *Wegner and Ernst*, 1983; *Okamoto et al.*, 2011; *Malvoisin et al.*, 2012; *Klein and McCollom*, 2013; *Godard et al.* 2013]. Powdered samples allow reactions to proceed to completion relatively quickly, but the feedback on permeability and porosity evolution was only determined in *Goddard et al.* [2013]. In contrast, using fractured rock samples as experimental material results in reactions not reaching complete stages, and limited available reactive surface area limits the progress of reaction [e.g. *Farough et al.*, 2015; *Klein et al.*, 2015]. These experiments provide insight into the interaction between chemical and physical processes during water-rock reactions in ultramafic rocks under hydrothermal conditions.

In section 2, a brief description of the sample lithologies, source locations and the preparation processes, experimental assembly and procedures is provided. *Farough et al.*, [2015] provide a more detailed description of the experimental details. Section 3 presents the results of the evolution of fracture aperture with time and determines the rate of transformation of olivine to serpentine. Section 4, discusses the results in the light of previous studies and their application to natural settings. Section 5 provides the conclusions.

2. Methodology

2.1. Description of samples and sample preparation

The experiments were performed on five different ultramafic rocks, four peridotites (TS, JC, ND, SQ) and one pyroxenite (BC). The peridotite samples contained 80-85% Mg-rich olivine and the pyroxenite sample contained 85% Mg-rich orthopyroxene. The samples contained less than 10% serpentine. Detailed descriptions of the samples are provided in Table 1. This suite of rock samples provides a good representation of the ultramafic rock types in the upper mantle

[*Bodinier and Godard*, 2004]. All samples were cored from hand-sized specimens to form cylinders with nominal diameter of 1.8 cm. After coring, samples were cut to length of 2.3-2.4 cm and end surfaces and circumferences were ground and hand-polished to assure no leakage of pore fluid between the sample and outer silver jacket (Figure 1a). *Farough et al.,* [2015] provides additional details on sample preparation.

2.2. Experimental setup and procedures

The experiments on fractured ultramafic rock samples used a flow-through high-pressure high-temperature triaxial machine (Figure 1b). The experiments results report effective permeability following Darcy's Law, by measuring the flow rate and pore-pressure difference across the sample [*Farough et al.*, 2015]. Then, assuming a parallel plate model for flow in a tensile fracture and independently measuring intact permeability, time-dependent changes in average fracture permeability and fracture aperture (see section 3.1) are calculated. More details of the calculation are provided in *Farough et al.*, [2015].

Polished thin sections of the cross section of the samples perpendicular to the fracture in the rock core were prepared. To characterize reactants and products, a variety of analytical techniques, such as X-Ray Diffraction, Electron Microprobe and Scanning Electron Microscope all housed in the department of Geosciences at Virginia Tech, were utilized.

3. **Results**

3.1. Rate of reduction in fracture aperture with time

The effective permeability, k_e, of the cylindrical samples with a through-going fracture can be treated in terms of layers of different permeability parallel to the flow direction [e.g., *Farough et al.*, 2015]:

$$k_e = \frac{k_m A_m + k_f A_f}{A_m + A_f} \quad (1)$$

where k_m is matrix permeability and k_f is fracture permeability (m^2), $A_f = 2rb$ (m^2) is the fracture cross sectional area where r is the radius of the sample and b is the average fracture aperture (m), and the total sample cross-sectional area is $A_m + A_f = \pi r^2$ (m^2). *Farough et al.*, [2015] showed that k_e ranged between 2.4E-16- 8.6E-18 (m^2) in the early stages of the experiments and 1.08E-18-2.2E-21 (m^2) towards the end of the experiments, thus resulting in a permeability decrease of each sample of approximately one to two orders of magnitude during experiments.

Assuming that k_f can be approximated using the cubic law for flow in a fracture represented by parallel plates [*Bear*, 1972; *Witherspoon et al.*, 1980], the fracture permeability can be written:

$$k_f = \frac{b^2}{12} \quad (2)$$

By incorporating equation (2) into equation (1):

$$k_e = \frac{k_m(\pi r^2 - 2rb) + \frac{b^2}{12}(2rb)}{\pi r^2} \quad (3)$$

Then using the measured values of k_e and k_m [*Farough et al.*, 2015], the fracture aperture b as a function of time for each experiment was calculated from equation (3). The results plotted in Figure 2 show that b initially ranged between 0.01 and 1 μm for the experiments and decreased, by as much as an order of magnitude during the experimental run. To model the reduction in aperture, an exponential function is fit to the data in (Figure 2):

$$b = b_0 e^{(-\frac{t}{t^*})} \quad (4)$$

where b_0 is the starting aperture and t* is the characteristic decay time of the exponential function in hours. The first few data points of the TS and SQ samples and a few data points from the end of the TS, ND and JC experiments have been removed from the modeling analysis, because they appear to represent a secondary process [*Farough et al.*, 2015]. The decay time of aperture varies by approximately a factor of 3 for the different samples, ranging from approximately 111 to 333 hours (Table 2). TS, JC and ND samples have better fits to an exponential function than SQ and BC, mainly because the latter have a strong initial decay in aperture, but all the samples follow a monotonic reduction, with a better fit towards the end compared to the beginning of the experiments.

3.2. Rate of transformation of reactants to products

Assuming that the rate of closure of the fracture is controlled by the overall transformation rate [e.g. *Bekri et al.*, 1997; *Detwiler et al.*, 2008; *Aharonov et al.*, 1998; *Farough et al.*, 2015], then the derivative of the fracture aperture b with time can be linked to the rate of the chemical

reactions taking place within the fracture. This includes primarily the dissolution of olivine and pyroxene along the fracture walls and in situ precipitation of serpentine. Taking the derivative of equation (4) yields:

$$\frac{db}{dt} = \frac{b_0}{t^*} e^{\left(-\frac{t}{t^*}\right)} \quad (5)$$

If one assumes the difference between the dissolution flux of reactants, J_r, and precipitation flux, J_p, on both walls of the fracture contribute to the rate of reduction in aperture then:

$$\frac{db}{dt} = -2\Delta J\, \Delta V_m \quad (6)$$

where $\Delta J = J_p - J_r$ is the difference between the dissolution of reactants and precipitation of products fluxes mol/m^2 s and $\Delta V_m = V_{mp} - V_{mr}$ is the difference in the molar volume between the products and reactants (Table 3). In the simplest form to estimate ΔV_m, I assume that only the most abundant mineral of each sample is a reactive phase; then in TS, JC, ND and SQ samples 2 moles of forsterite would produce 1 mole of serpentine and brucite and in the BC sample 6 moles of enstatite would produce 1 mole of serpentine and talc. For simplicity I use room temperature estimates of the molar volumes, as the effects of temperature and pressure changes is small under the imposed experimental conditions. Thus from Table 2, ΔV_m for forsterite and enstatite reactions at room pressures and temperatures is ~4.2E-5 and ~2.6E-5 m^3/mol respectively. The mineralogical analysis [*Farough et al.*, 2015] along with fluid chemistry data (Appendix 1) shows that the extent of dissolution reactions in our experiments is incomplete, because brucite

and talc were not detected by electron microprobe. Thus if no brucite was produced ΔV_m for forsterite reactions ~1.8E-5 m^3/mol, but for the enstatite reaction ΔV_m will be negative.

From equations (5) and (6) ΔJ as a function of time can be estimated from:

$$\Delta J = \left(\frac{b_0}{2\Delta V_m t^*}\right) e^{-\frac{t}{t^*}} \quad (7)$$

Estimated values of ΔJ range between ~ 10^{-8}-10^{-9} (mol/m^2s) initially and decrease about one order of magnitude during the experiments (Table 4). For olivine reactions, using the smaller value of ΔV_m would increase the estimated reaction rate by approximately a factor of 2. If talc is not a product of the reaction in the BC sample, then the observed decrease in fracture permeability would appear to not have been caused by hydration reactions but by other processes such as the movement of loose grains [e.g. *Farough et al.*, 2015]. The slowing of the transformation rate with increasing time likely occurs because the reactive surface area of reactants decreases with time as precipitates form on the walls of the fracture. If reactive surface area were completely covered with precipitates, the rate of transformation would be limited by the rate of diffusion of water across the reaction products to fresh unaltered [*Macdonald and Fyfe*, 1985].

Martin and Fyfe [1970] estimate the rate constant, *K*, for serpentinization of olivine with grain size 58–79 μm at 260˚C to be 1E-6 s^{-1}. To be able to compare ΔJ with *K*, we can write *K* as:

$$K = \Delta J \times S_m \times W_m \quad (8)$$

where $S_m = A_g/M_g$ is the reactive surface area per unit mass of reactant, $A_g = AGS^2$ reactive surface of each grain m^2 (Table 1), $M_g = \rho_g \times AGS^3$ is the mass of reactants kg , W_m is the molecular weight kg/mol. Equation (8) assumes that the entire fracture surface is reactive. Values used for the parameters in equation (8) are provided in Table 5. From equation (8), estimates of K in our experiments initially range between 1.E-5 and 1.E-7 s^{-1} with about an order of magnitude drop during experiments (Table 5). These results fall in approximately the same range as estimates of *Martin and Fyfe* [1970]. *Wegner and Ernst* [1983], and *Lafay et al.*, [2012] had similar results. A recent study by *Malvoisin et al.*, [2012] found much slower rates for the reactions; however, they used production of magnetite as a tracer for the progress of reaction. Magnetite production occurs after multiple stages of reaction [*Beard et al.*, 2009; *Bach et al.*, 2006], but in our experiments the reactions didn't progress far enough to produce magnetite and the rates that are being reported here are for the very initial stages of dissolution of olivine and pyroxene and precipitation of serpentine. The effective rate constant determined in this study is similar to that of *Martin and Fyfe* [1970] experiments on powdered samples, which is surprising given the limited surface area of reaction in *Farough et al.*, [2015] experiments. The high effective rate suggests that reactants may block critical fracture interconnections leading to a rapid reduction in mean crack aperture determined from the parallel plate law.

Estimated rate of transformation tends to support the assumption in this model and discussion of *Farough et al.*, [2015] that the evolution of fracture permeability is largely controlled by dissolution and precipitation processes, at least while there is sufficient surface area available for reaction. The rate of reaction in olivine rich samples is faster than that for the pyroxenite sample, which is consistent with prior measurements showing that the rate of enstatite dissolution at such pressure and temperature conditions is slower than that of olivine [*Okamoto et al.*, 2011].

4. Applications to natural settings

This study couples dissolution/precipitation processes to evolution of fracture aperture during serpentinization reactions. In these experiments, the rate of transformation of olivine to serpentine along the walls of a tensile fracture in cores of ultramafic rocks is fastest at the early stages and decreases monotonically as reactive surface areas become covered under precipitates. As the transformation from olivine to serpentine occurs along the fracture walls, the fracture aperture closes and the fracture permeability decreases. This means that the geochemical evolution of the system controls physical evolution. An analogous process occurs during diagenesis in feldspathic sandstones [*Aharonov et al.*, 1998].

In the oceanic crust, faults and fractures are the main path for fluid circulation, thus evolution of their physical and fluid transport properties during chemical alteration is important for progress of hydration reactions. This study suggests that at early stages of serpentinization reactions where the transformation rate is high, dissolution of olivine and pyroxene have a leading role in permeability of the flow path and as the reaction progresses and less reactive surface area becomes available, rate of transformation nominally decreases and precipitation of serpentine and other products becomes the leading process in evolution of permeability of the flow path. Such mechanisms in permeability reduction can cause seals and zone of high fluid pressure in the oceanic crust.

5. Conclusions

In this chapter I report the rate of transformation of olivine and pyroxene to serpentine in serpentinization reactions during which fracture aperture and permeability are reduced as a result of mineral dissolution and precipitation. The model is applied to the experimental results of *Farough et al*., [2015] and aims to understand the linkages between the reaction rate and the corresponding changes in fracture permeability. The results suggest that dissolution of the reactants and precipitation of serpentine within the fracture is the dominant mechanism in reducing fracture aperture with time [*Farough et al*., 2015]. Similar to reduction in permeability and aperture of the system, rate of transformation is fastest early in the experiments and declines as surface area for reaction becomes limited.

6. References

Abrajano, T., N. Sturchio, J. Bohlke, G. Lyon, R. Poreda, and C. Stevens (1988), Methane-hydrogen gas seeps, Zambales Ophiolite, Philippines: Deep or shallow origin?, *Chemical Geology*, 71(1), 211-222.

Aharonov, E., E. Tenthorey, and C. H. Scholz (1998), Precipitation sealing and diagenesis: 2. Theoretical analysis, *Journal of Geophysical Research*, *103*(B10), 23969–23981, doi:10.1029/98JB02230.

Allen, D. E., and W. E. Seyfried (2003), Compositional controls on vent fluids from ultramafic-hosted hydrothermal systems at mid-ocean ridges: An experimental study at 400°C, 500 bars, *Geochimica et Cosmochimica Acta*, *67*(8), 1531-1542.

Andreani, M., L. Luquot, P. Gouze, M. Godard, E. Hoise, and B. Gibert (2009), Experimental study of carbon sequestration reactions controlled by the percolation of CO2-rich brine through peridotites, *Environmental science & technology*, *43*(4), 1226-1231.

Bach, W., H. Paulick, C. J. Garrido, B. Ildefonse, W. P. Meurer, and S. E. Humphris (2006), Unraveling the sequence of serpentinization reactions: petrography, mineral chemistry, and petrophysics of serpentinites from MAR 15°N (ODP Leg 209, Site 1274), *Geophysical Research Letters*, 33, L13306, doi:10.1029/2006GL025681.

Barnes, I., J. O'neil, and J.-J. Trescases (1978), Present day serpentinization in New Caledonia, Oman and Yugoslavia, *Geochimica et Cosmochimica Acta*, *42*(1), 144-145.

Beard, J. S., B. R. Frost, P. Fryer, A. McCaig, R. Searle, B. Ildefonse, P. Zinin, and S. K. Sharma (2009), Onset and Progression of Serpentinization and Magnetite Formation in Olivine-rich Troctolite from IODP Hole U1309D, *Journal of Petrology*, *50*(3), 387-403.

Bekri, S., J.-F. Thovert, and P. Adler (1997), Dissolution and deposition in fractures, *Engineering Geology*, *48*(3), 283-308.

Bodinier, J., and M. Godard (2004), Treatise on Geochemistry, Volume 2: The Mantle and Core.

Cann, J., D. Blackman, D. Smith, E. McAllister, B. Janssen, S. Mello, E. Avgerinos, A. Pascoe, and J. Escartin (1997), Corrugated slip surfaces formed at ridge-transform intersections on the Mid-Atlantic Ridge, *Nature*, *385*(6614), 329-332.

Cannat, M. (1993), Emplacement of mantle rocks in the seafloor at mid-ocean ridges, *Journal of Geophysical Research*, *98*(B3), 4163-4172.

Carlson, R. (2001), The abundance of ultramafic rocks in Atlantic Ocean crust, *Geophysical Journal International*, *144*(1), 37-48.

Coleman, R. G. (1971), Petrologic and geophysical nature of serpentinites, *Geological Society of America Bulletin*, *82*(4), 897-918.

Detwiler, R. L. (2008), Experimental observations of deformation caused by mineral dissolution in variable-aperture fractures, *Journal of Geophysical Research*, *113*, B08202, doi:10.1029/2008JB005697.

Dyment, J., J. Arkani-Hamed, and A. Ghods (1997), Contribution of serpentinized ultramafics to marine magnetic anomalies at slow and intermediate spreading centres: insights from the shape of the anomalies, *Geophysical Journal International*, *129*(3), 691-701.

Escartín, J., G. Hirth, and B. Evans (2001), Strength of slightly serpentinized peridotites: Implications for the tectonics of oceanic lithosphere, *Geology*, *29*(11), 1023-1026.

Escartín, J., C. Mével, C. J. MacLeod, and A. M. McCaig (2003), Constraints on deformation conditions and the origin of oceanic detachments: The Mid-Atlantic Ridge core complex at 15°45′N, *Geochemistry Geophysics Geosystems*, *4*, 1067, doi:10.1029/2002GC000472.

Evans, B. W. (1977), Metamorphism of alpine peridotite and serpentinite, *Annual Review of Earth and Planetary Sciences, 5*, 397-447.

Faccenda, M., T. V. Gerya, and S. Chakraborty (2008), Styles of post-subduction collisional orogeny: Influence of convergence velocity, crustal rheology and radiogenic heat production, *LITHOS*, *103*(1-2), 257-287.

Godard, M., L. Luquot, M. Andreani, and P. Gouze (2013), Incipient hydration of mantle lithosphere at ridges: A reactive-percolation experiment, *Earth and Planetary Science Letters*, *371–372*, 92-102.

Hilairet, N., and B. Reynard (2009), Stability and dynamics of serpentinite layer in subduction zone, *Tectonophysics*, *465*(1-4), 24-29.

Hövelmann, J., H. Austrheim, and B. Jamtveit (2012), Microstructure and porosity evolution during experimental carbonation of a natural peridotite, *Chemical Geology*, *334*, 254-265.

Hyndman, R. D., and S. M. Peacock (2003), Serpentinization of the forearc mantle, *Earth and Planetary Science Letters*, *212*(3-4), 417-432.

Janecky, D., and W. Seyfried Jr (1986), Hydrothermal serpentinization of peridotite within the oceanic crust: experimental investigations of mineralogy and major element chemistry, *Geochimica et Cosmochimica Acta*, *50*(7), 1357-1378.

Klein, F., N. G. Grozeva, J. S. Seewald, T. M. McCollom, S. E. Humphris, B. Moskowitz, T. S. Berquó, and W.-A. Kahl (2015), Fluids in the Crust. Experimental constraints on fluid-rock reactions during incipient serpentinization of harzburgite, *American Mineralogist*, *100*(4), 991-1002.

Malvoisin, B., F. Brunet, J. Carlut, S. Rouméjon, and M. Cannat (2012), Serpentinization of oceanic peridotites: 2. Kinetics and processes of San Carlos olivine hydrothermal alteration, *Journal of Geophysical Research*, *117*, B04102, doi:10.1029/2011JB008842.

Manning, C. E. (1995), Phase-equilibrium controls on SiO2 metasomatism by aqueous fluid in subduction zones: Reaction at constant pressure and temperature, *International Geology Review*, *37*(12), 1074-1093.

Martin, B., and W. Fyfe (1970), Some experimental and theoretical observations on the kinetics of hydration reactions with particular reference to serpentinization, *Chemical Geology*, *6*, 185-202.

Miller, D. J., and N. I. Christensen (1997), Seismic velocities of lower crustal and upper mantle rocks from the slow-spreading Mid-Atlantic Ridge, south of the Kane Transform Zone (MARK), *Proceedings of the Ocean Drilling Program*, Scientific results, ISSN 0884-5891, *153*, 596 p., 45 ref., 437-454.

Neal, C., and G. Stanger (1983), Hydrogen generation from mantle source rocks in Oman, *Earth and Planetary Science Letters*, *66*, 315-320.

Okamoto, A., Y. Ogasawara, Y. Ogawa, and N. Tsuchiya (2011), Progress of hydration reactions in olivine–H2O and orthopyroxenite–H2O systems at 250°C and vapor-saturated pressure, *Chemical Geology*, *289*(3-4), 245-255.

Oze, C., L. C. Jones, J. I. Goldsmith, and R. J. Rosenbauer (2012), Differentiating biotic from abiotic methane genesis in hydrothermally active planetary surfaces, *Proceedings of the National Academy of Sciences*, *109*(25), 9750-9754.

Reston, T. J. (2009), The structure, evolution and symmetry of the magma-poor rifted margins of the North and Central Atlantic: A synthesis, *Tectonophysics*, *468*(1-4), 6-27.

Rupke, L. (2004), Serpentine and the subduction zone water cycle, *Earth and Planetary Science Letters*, *223*(1-2), 17-34.

Schmidt, K., A. Koschinsky, D. Garbeschonberg, L. Decarvalho, and R. Seifert (2007), Geochemistry of hydrothermal fluids from the ultramafic-hosted Logatchev hydrothermal field, 15°N on the Mid-Atlantic Ridge: Temporal and spatial investigation, *Chemical Geology*, *242*(1-2), 1-21.

Seyfried Jr, W., and W. Dibble Jr (1980), Seawater-peridotite interaction at 300 C and 500 bars: implications for the origin of oceanic serpentinites, *Geochimica et Cosmochimica Acta*, *44*(2), 309-321.

Seyfried, W. E., D. I. Foustoukos, and Q. Fu (2007), Redox evolution and mass transfer during serpentinization: An experimental and theoretical study at 200°C, 500bar with implications for ultramafic-hosted hydrothermal systems at Mid-Ocean Ridges, *Geochimica et Cosmochimica Acta*, *71*(15), 3872-3886.

Skelton, A., and M. Jakobsson (2007), Could peridolite hydralion reactions have provided a contributory driving force for Cenozoic uplift and accelerated subsidence along the margins of the North Atlantic and Labrador Sea?, *NORSK GEOLOGISK TIDSSKRIFT*, *87*(1/2), 21.

Smith, D. K., J. Escartin, H. Schouten, and J. R. Cann (2008), Significant processes in seafloor formation at slow-spreading mid-ocean ridges (Mid-Atlantic Ridge, 13°-15°N), *Geochemistry Geophysics Geosystems*, 9, Q03003, doi:10.1029/2007GC001699.

Wegner, W. W., and W. Ernst (1983), Experimentally determined hydration and dehydration reaction rates in the system MgO–SiO2–H2O, *American Journal of Science*, *283*, 151-180.

Witherspoon, P., J. Wang, K. Iwai, and J. Gale (1980), Validity of cubic law for fluid flow in a deformable rock fracture, *Water Resources Research*, *16*(6), 1016-1024.

Zonenshain, L., M. Kuzmin, A. Lisitsin, Y. A. Bogdanov, and B. Baranov (1989), Tectonics of the Mid-Atlantic rift valley between the TAG and MARK areas (26–24 N): evidence for vertical tectonism, *Tectonophysics*, *159*(1), 1-23.

7. Figures

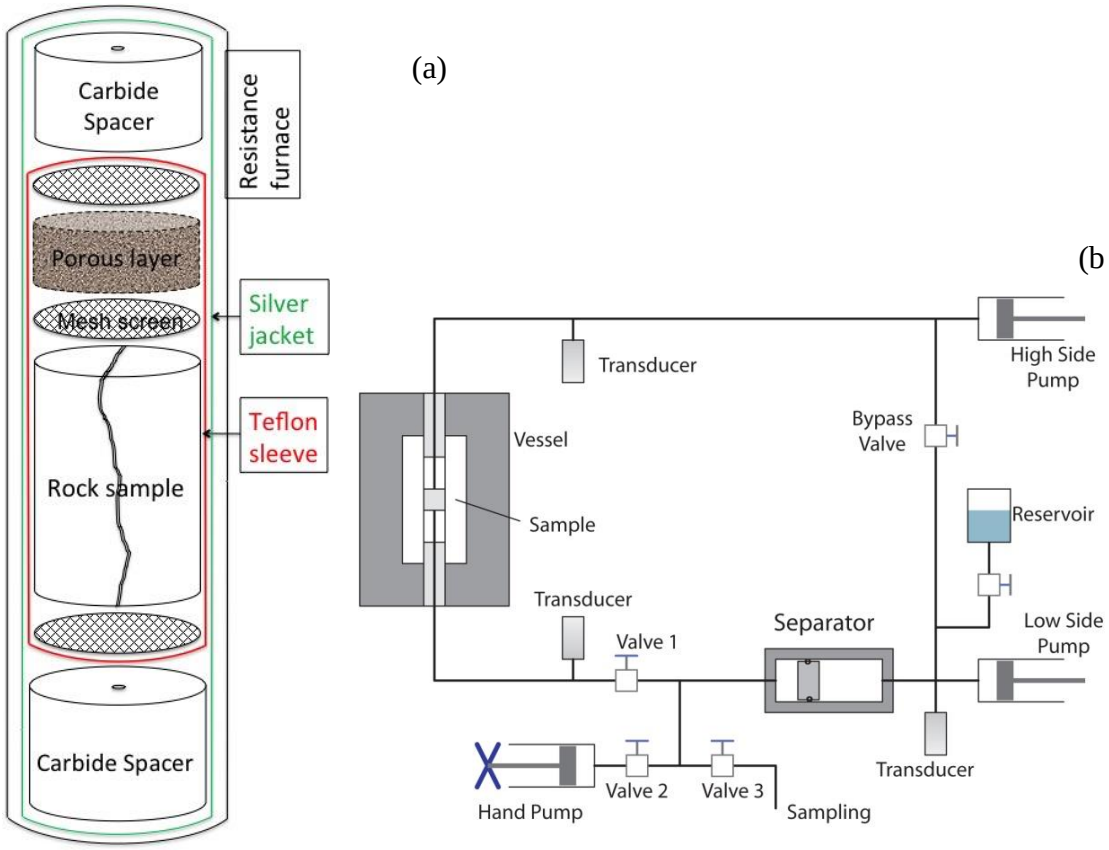

Figure (1): (a) Schematic of the assembly for the experiments at elevated temperatures. (b) The setup of the whole system. The solute-free fluid is stored in the reservoir. If the bypass valve is open, fresh water is let in the system. The high-side pump directs the fluid to the sample. From *Farough et al.*, [2015]

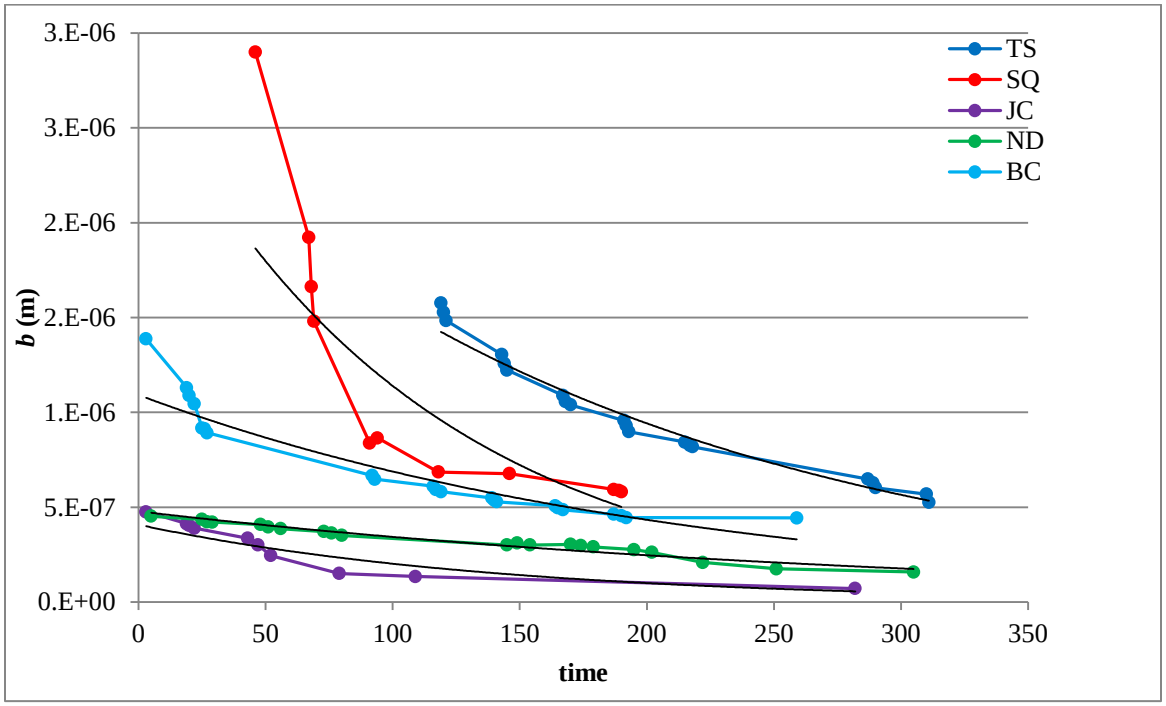

Figure (2): Evolution of effective aperture *b* of the samples during the experiments, solid black lines show the best fitting exponential curves (Table 3).

8. Tables

Table (1): Description of the samples used for the experiments [*Farough et al.*, 2015].

Sample		Locality	AGS* (mm)	Mineral assemblage**	
				Major phase (~80-90%)***	Other phases (~10-20%)
Dunite	TS	Twin Sisters, WA	0.2-5	Olivine ($Mg_{1.8}$, $Fe_{0.2}$)	Serpentine(1-2%), opx (5-10%), chromium spinel (<2%)
	JC	Jackson County, NC	0.1-0.3	Olivine ($Mg_{1.7}$, $Fe_{0.3}$)	Serpentine(2-4%), talc (<1%), actinolite/tremolite (2-5%), chlorite (<1%), chromium spinel (2-5%),
	ND	Spruce Pine, NC	0.1-0.6	Olivine ($Mg_{1.8}$, $Fe_{0.2}$)	Serpentine(5-8%), talc (2%), chlorite (2%), actinolite/tremolite (2%)
Harzburgite	SQ	1.5 km southwest of San Quintin, Baja, Mexico	0.05-1	Olivine ($Mg_{1.64}$, $Fe_{0.36}$)	Serpentine(<1%),opx (15%), chromium spinel (2-5%)
Pyroxenite	BC	east of Bushveld complex, South Africa	0.05-0.2	Orthopyroxene ($Mg_{0.56}$, $Fe_{0.44}$)	Serpentine (2-4%), plagioclase (2-4%), talc (2%), olivine (5%)

*Average Grain Size

** Compositions are provided using XRD, Rigaku's PDXL software (version 1.8)

***what is introduced as reactants in section (3.2).

Table (2): The decay time and corresponding initial aperture values, ratio of standard error (STD error) to the estimated value and and R^2 in each sample.

	b_0 (m x 10^{-6})	STD error/estimate	t*(hrs)	STD error/estimate	R^2
TS	3	0.003	200	0.042	0.97
SQ	3	0.016	111.1	0.178	0.77
JC	0.4	0.007	143	0.143	0.86
ND	0.5	0.002	333	0.060	0.93
BC	1	0.003	200	0.070	0.91

Table (3): Molar volumes of minerals involved in the reactions.

	Mineral	$V_m \times 10^{-5}$ (m^3/mol)*
Reactants	Olivine	~4.5
	Orthpyroxene	~2.5
Products	Serpentine	~10.8
	Brucite	~2.4
	Talc	~6.8

* http://database.iem.ac.ru/mincryst/

Table (4): Estimated difference between the dissolution flux of olivine and pyroxene and precipitation flux of serpentine based on rate of aperture closure.

	time (hrs)	b (m x 10^{-6})	ΔV (m^3/mol x 10^{-5})	ΔJ (mol/m^2s x 10^{-8})
TS	119	1.58	~4.20	2.74
	310	0.57		1.05
SQ	46	2.9	~4.20	5.9
	190	0.58		1.61
JC	3	0.47	~4.20	0.90
	282	0.07		0.13
ND	5	0.45	~4.20	0.49
	305	0.16		0.19
BC	3	1.39	~2.60	1.63
	259	0.443		0.45

Table (5): Parameters to estimate reaction rate

	time (hrs)	AGS (m x10^{-4})	ρ (kg/m^3)	Sm (m^2/kg)	Vm (m^3/mol x10^{-4})	Wm (kg/mol)	K (s^{-1}x10^{-6})
TS	119	26	3330	4.8E-05	5.0	0.14	1.6
	310			4.8E-05			0.62
SQ	46	0.52		2E-06			17
	190			2E-06			4.7
JC	3	2.0		2.8E-07			6.9
	282			2.8E-07			0.98
ND	5	3.5		8.7E-07			2.1
	305			8.7E-07			0.86
BC	3	1.25	3200	7.8E-08	2.5	0.10	24
	259			7.8E-08			6.6

Appendix

A.1. Elemental analysis of pore fluid

Each collected fluid sample was diluted with 1% nitric acid to a total volume of 3 cm^3 and was analyzed for major cations (Mg, Fe) and silica using an Inductively Coupled Plasma Atomic Emission Spectrometer (ICP-AES). The raw data of the ICP-AES (mg/L) was converted using calculations of the dilution factor of the nitric acid for each sample to get the real concentrations, then each concentration was converted to Molar (M) concentrations.

The fluid chemistry data for TS, SQ, ND and BC samples are plotted in Figure (A.1a, b, c, d, e). In the JC sample, the initially low fracture permeability and the fast drop resulted in very few fluid sample collections, thus no fluid chemistry data are reported for the JC experiment. The Si concentration is orders of magnitude higher than Mg, which relates to the Mg/Si ratio of the dissolving and precipitating phases but is not consistent with the compositions of these phases. The high concentration of Si compared to the other elements and also the trend of increase, followed by a monotonic decrease in all of the samples is very noticeable.

The concentration of Fe in all of the samples except TS, peaks in early stages of the high temperature experiments Figure (A.1a). The concentration of Mg and Fe in all the fluid samples is an order of magnitude less than Si and all of the samples tend to reach a constant value of Mg towards the end of the experiments Figure (A.1b). Concentration of Si, similar to Fe, in most of the samples peaks in early stages of the experiments before decreasing monotonically. SQ and BC have noticeably higher Si concentrations than the other samples Figure (A.1c). Concentration of Ca, is in the same order of magnitude as Mg. Towards the end of the experiments,

concentration of Ca becomes constant Figure (A.1d). I did not obtain the Ca data for the discharge of TS sample.

In the SQ samples, all the elements monotonically decrease after the peak near the start in the high temperature experiment. Evolution of the concentrations of all the elements in the BC sample through the experiment is similar, showing an early peak and reaching equilibrium towards the end of the experiment. ND has a relatively high Fe concentration. In The TS sample dissolution of Fe bearing phases start much later in the experiment. The analysis of the BC sample, which exhibits considerably higher Fe may indicate precipitation of Fe-rich phase. There is no evidence of brucite or talc precipitation in the samples based on microprobe analysis [*Farough et al.*, 2015].

The (Mg+Fe)/Si of the collected pore fluid is shown in Figure (A.1e). If olivine and pyroxene dissolve the (Mg+Fe)/Si of the solution is 2 and 1 respectively and if serpentine precipitates (Mg+Fe)/Si is 1.5. The (Mg+Fe)/Si of the pore fluid does not relate to any of these processes, this could be as a result of dissolution of Si-bearing minor phases in the samples such as talc, actinolite/tremolite or contamination of the pore fluid with material precipitated in pipes from previous experiments.

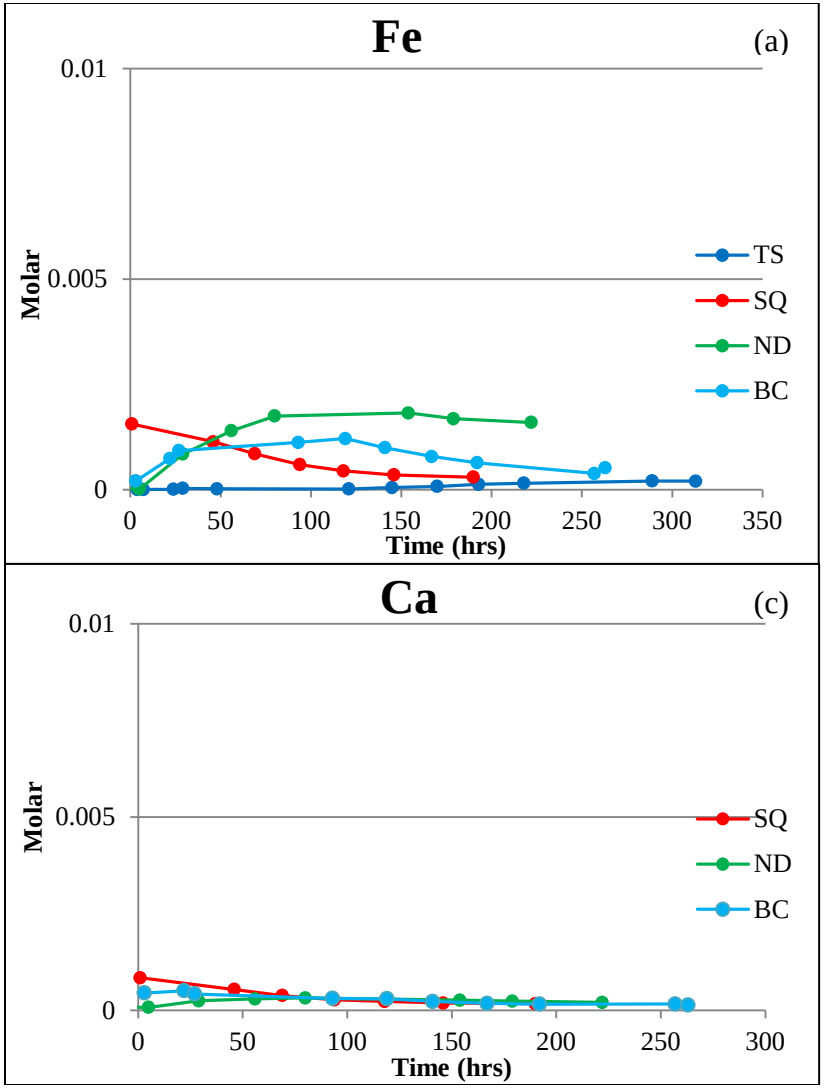
Fe
(a)
0.01
0.005
0
Molar
0
50
100
150
200
250
300
350
Time (hrs)
TS
SQ
ND
BC

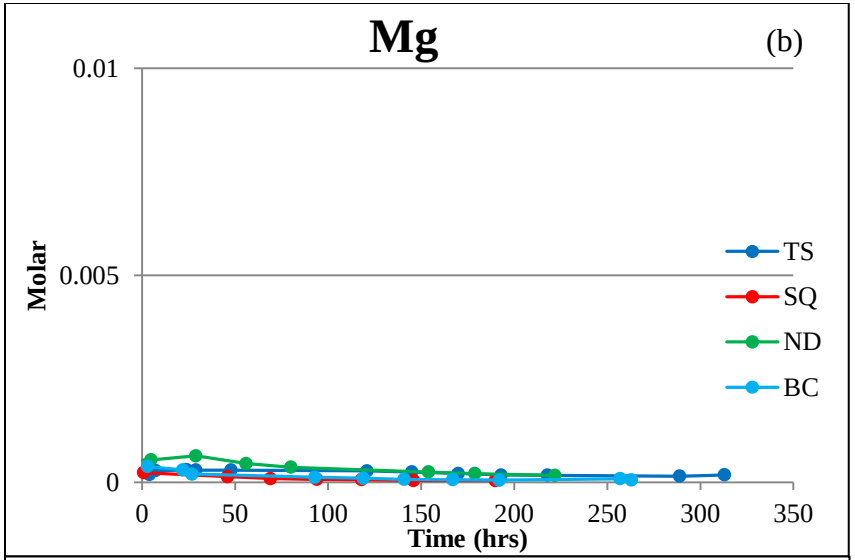
Mg
(b)
0.01
0.005
0
Molar
0
50
100
150
200
250
300
350
Time (hrs)
TS
SQ
ND
BC

Ca
(c)
0.01
0.005
0
Molar
0
50
100
150
200
250
300
Time (hrs)
SQ
ND
BC

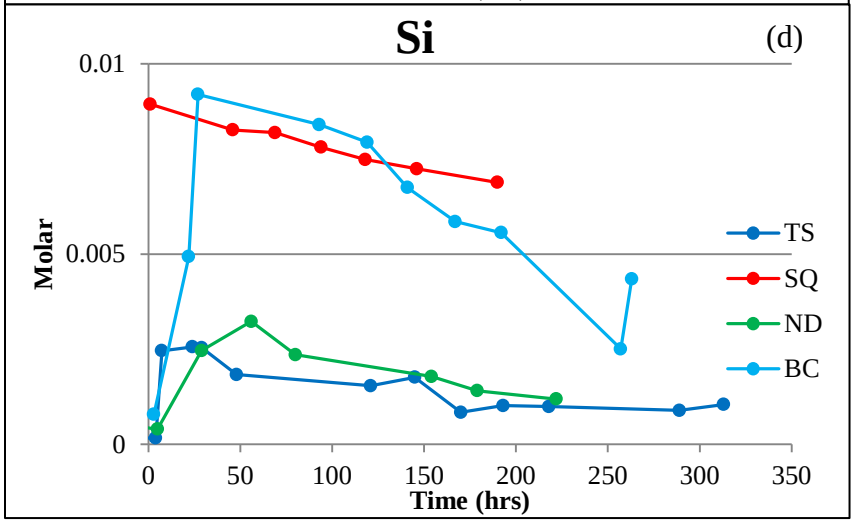
Si
(d)
0.01
0.005
0
Molar
0
50
100
150
200
250
300
350
Time (hrs)
TS
SQ
ND
BC

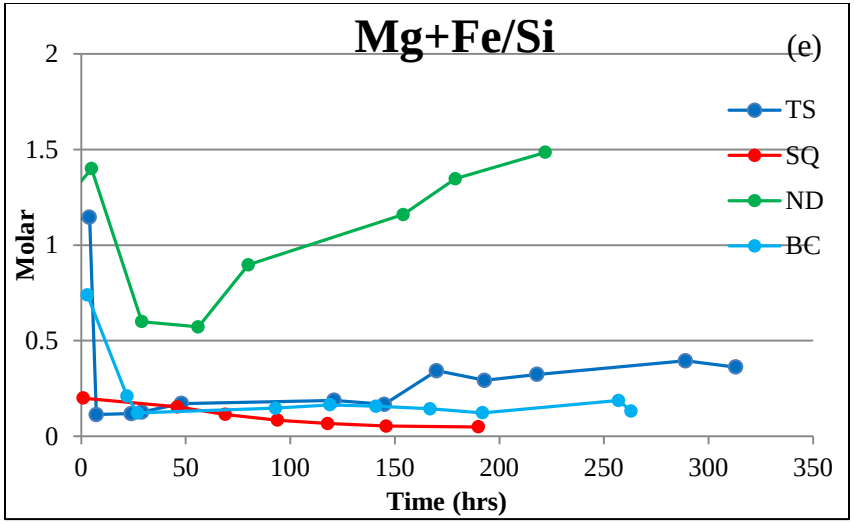

Figure A.1. Composition of pore fluid collected during the experiments.(a) concentration of Fe, (b) Mg, (c) Si, (d) Ca, in the collected pore fluid samples (e) Mg+Fe/Si ratio

Chapter 4: Estimates of Permeability, Porosity, Density and Correlations between These Parameters in Some Dunites and Pyroxenites

Abstract

There is little known about the pressure dependency of physical properties of ultramafic rocks, in this chapter the results of a study focused on measuring fluid flow properties of ultramafic rocks is presented. flow through experiments were performed on intact samples of ultramafic rocks at room temperature and effective pressures of 10, 20 and 30 MPa and the intact permeability was measured as a function of effective pressure. Also porosity and density of the samples were measured.

The pressure sensitivity coefficient of permeability was estimated in the range of 0.05-0.14 MPa^{-1} by fitting the permeability versus pressure to an exponential curve. Using the measured porosity and permeability at 0.1 MPa and assuming a power law correlation between them, the ratio of interconnected porosity to total porosity is estimated to be small and the permeability is dominantly controlled by microcracks. Using the density and porosity measurements, the degree of alteration of the samples is estimated. Samples with high density and pressure dependent permeability have a smaller degree of alteration than those with lower density and pressure dependency.

1. Introduction

Physical, storage and transport properties of Earth's crustal rocks are of fundamental importance for nearly all aspects of earth science research. For example, density and seismic velocity provide key insights into earth's evolution and structure. Porosity of crustal rocks provides key information on the storage capacity and behavior of subsurface fluid reservoirs and their response to temperature and pressure in the earth's crust. Permeability is the main parameter that controls fluid flow and the transport of heat and mass in a variety of crustal environments. For example, permeability and porosity have a key role in fluid flux and geochemical transport in magmatic system at mid oceanic ridges [e.g. *Lowell*, 1975; *Bickle and Teagle*, 1992; *Elderfield et al.*, 1999] and subduction zones [e.g. *Hyndman et al.*, 1993; *Gamage et al.*, 2011], as well as in enhanced geothermal systems [e.g. *Taron and Elsworth*, 2009; *Pruess*, 2004]. Mass, heat and chemical transport in fault zones plays a significant role in global seismicity [e.g. *Byerlee*, 1993; *Sleep and Blanpied*, 1994].

Porosity and permeability of sedimentary rocks have been widely studied because of their importance as groundwater aquifers and hydrocarbon reservoirs [e.g. *Friedman and Sanders*, 1978; *Thompson et al.*, 1987; *Tiab and Donaldson*, 2011]. Ultramafic rocks have received less attention. Most of the studies on physical properties of ultramafic rocks have focused on seismic properties and stress-strain characteristics. For example, *Christensen* [1974, 1978, and 1996] reported average densities, seismic velocities and Poisson's ratios over a range of hydrostatic pressures on samples from different ophiolite complexes. *Hyndman and Drury* [1976] determined seismic velocities, electrical resistivity, bulk and grain density, porosity and water content, and thermal conductivity of serpentinized peridotites from Deep-Sea Drilling Project

(DSDP) LEG 37 on the mid-Atlantic ridge near 37˚N. *Byerlee* [1968] presented strength and deformation characteristics of Spruce Pine dunites; *Raleigh and Paterson* [1965] provided stress-strain curves for serpentinites. *Gowd* [1967] studied the failure of pyroxenties and peridotites under uniaxial compression, and *Rao and Ramana* [1974] investigated the dilatancy of ultramafic rocks during fracturing and report density, porosity and seismic velocity of a range of ultramafic rocks from India. None of these studies estimated alteration in their samples; but *Escartin et al.*, [2001] measured strength as a function of pressure, and the nominally non-dilatant mode of brittle deformation of slightly serpentinized peridotites. They also determined the influence of serpentine content on the strength and the style of deformation of peridotites.

Fluid transport properties of ultramafic rocks and their pressure dependency are still poorly understood, a complicated network of fractures dominates permeability and porosity. *Macdonald and Fyfe*, [1985] estimated permeability of partially serpentinized peridotites near room temperature and pressure to be in the range of 10^{-23} to 10^{-24} m^2. *Hirose and Hayman*, [2008] report permeability values of 10^{-19} m^2 for a serpentinized dunite from Hole 1309D from the Integrated Ocean Drilling Program (IODP) at the Atlantis Massif, Mid-Atlantic Ridge, 30°N.

Regions of high pore pressure in geologic settings, such as overthrusting, diapirism and hydrothermal vein formation, can be as a result of changes in stress from mechanical overload [*Shi and Wang*, 1986], which results in stress dependency of fluid transport properties. In addition to lithostatic pressure, thermal and tectonic stresses in the Earth also affect fluid transport properties of the crust [e.g. *Sibson*, 1994]. It is recognized that the effect of pressure on permeability is much larger for crack-controlled permeability than for permeability resulting from interconnected primary porosity [e.g., *Walsh*, 1965], hence the pressure dependency of permeability in ultramafic rocks is of interest.

Understanding pressure dependency of fluid transport properties of ultramafic rocks is needed to evaluate accessibility to atypical and deep petroleum systems in and around igneous rocks [e.g. *Schutter,* 2003*; Farooqui et al.*, 2009*; Griffith*, 2012]. It is also important in production optimization of geothermal reservoirs [e.g. *Milsch et al.*, 2009; *Darnet et al.*, 2006*; Bjornsson and Stefansson*, 1987]. In fault zones hosted in ultramafic rocks, fluid transport properties affect fault instability and strength [*Lachenbruch* 1980; *Andrews* 2002] and results in generation of low-frequency earthquakes [*Suzuki and Yamashita* 2009; *Ito and Obara* 2006; *Tanikawa et al.*, 2014].

In addition to understanding the effect of pressure on permeability in ultramafic rocks, it is also useful to determine the linkage between permeability and porosity, which provides information on the ratio of effective to non effective porosity. The Kozeny–Carman relationship, which suggests a power law between porosity and permeability, is most used in studies of flow in porous media [*Kozeny*, 1927; *Carman*, 1937]. Because of the importance of sedimentary rocks to petroleum geology and reservoir characterization, many studies were focused on pore controlled fluid transport in sedimentary rocks rather than fracture controlled rocks such as ultramafic rocks. For example, *Bourbie et al.*, [1985] investigated hydraulic properties of Fontainebleau Sandstone as a function of porosity. In numerous studies porosity-permeability relationships have been developed as power law function, but with significant differences. *Kühn* [2004] summarizes the different relationships and shows that most models are consistent with a cubic function [*Bear*, 1972] (Figure 1). But studies of sulfide chimney deposits at mid-ocean ridges [*Zhu et al.*, 2007] suggest a higher power correlation ($k \sim \varphi^9$).

In this chapter, I present the results of experiments measuring the permeability of a number of ultramafic rock samples at effective pressures of 10, 20, and 30 MPa. Results show that the

permeability trend fits an exponential function, and the pressure sensitivity of permeability and microcrack apertures are estimated. By using dry and saturated weights and volume of the samples porosity and density are determined; and based on these data, the degree of alteration of each sample is estimated. Following the common power-law relationship between permeability-porosity, the interconnected porosity of the samples is analyzed.

2. Sample Description and Sample Preparation

The experiments were performed on intact cores of four different ultramafic rocks, three peridotites and one pyroxenite. Detailed descriptions of the samples are provided in Table 1. All experimental cores had a diameter of 1.8 cm, and length of 0.9 to 1.3 cm. After coring, samples were ground and hand-polished to assure no leakage of pore fluid between the sample and the housing jacket. More detailed description of samples and the preparation procedure is provided in *Farough et al*., [2015].

3. Experimental Setup and Procedures

Flow-through experiments on intact samples of ultramafic rocks were performed to estimate matrix permeability k_m at room temperature, using observed flow rate and assuming that Darcy's Law holds. The methodology of these experiments is the same as *Morrow et al.* [2014], except that in this study de-ionized water was utilized as pore fluid. Porous Berea sandstone wafers (19 mm diameter by 0.65 mm thickness), with high permeability ($> 10^{-15}$ m^2) were placed on the top and bottom of the samples to provide a uniform pore pressure to the upstream and downstream sample faces. Because the permeability of Berea sandstone is many orders of magnitude higher

than that of ultramafic rocks, it can be neglected in calculations of permeability (Figure 2). The sample assembly was placed in a latex jacket and secured to steel end plugs. Flow rate was measured under steady flow conditions driven by a pore pressure gradient of 4 MPa. Measurements were made at increasing confining pressures, P_c, of 12, 22, 32 MPa and a average pore pressure, P_p, of 2 MPa resulting in increasing effective pressures, $P_e = P_c - P_p$, of 10, 20 and 30 MPa in order to evaluate the response of the samples to increasing overburden in the upper crust to ~ 2 km depth) (Table 2).

Porosity of the same cores was estimated by measuring the difference between the dry and immersed weight in water. Using the dry weight, porosity and volume measurements, density of the porous samples and grain density were estimated.

4. Results

4.1. Matrix Permeability

The matrix permeability of each sample k_m is estimated using Darcy's Law:

$$\frac{Q}{A} = -\frac{k_m}{\eta}\frac{\Delta P_p}{L} \quad (1)$$

where Q is the volumetric flow rate m^3/s under steady flow conditions, A is the cross-sectional area of the cylinder m^2, η is the dynamic viscosity of the fluid Pa-s, L is the sample length m and ΔP_p is the pore-pressure difference applied across the sample MPa. Figure 3 shows how the permeability of each sample responds to increasing P_e. For each of the samples, k_m ranged between 1.7E-22 to 6.8E-22 at 10 MPa and decreased to 2.03E-22 to 3.14E-23 at 30 Mpa.

Increasing the effective pressure to 30 MPa, results in an order of magnitude drop in k_m of the samples, except for ND.

4.2. Pressure Sensitivity Coefficient of Matrix Permeability

The best fit equation to evolution of matrix permeability vs. effective pressure is:

$$k_m = k_{m_0} exp(-\gamma_k P_e) \quad (2)$$

where k_{m_0} is the initial matrix permeability of the samples m^2. The pressure sensitivity coefficient γ_k ranges between 0.05-0.14 MPa^{-1} (Table 3). I also find that permeability of TS and BC samples is more sensitive to changes in effective pressure than ND and JC. I extrapolate the data to estimate k_m at room pressure (1 atm) and the values range between 4.0E-22 to 3.0E-21.

4.3. Density

The density of the samples was estimated by dividing weight of the dry sample by the volume. Measured density ρ values ranged between 2780 kg/m^3 for ND sample to 3190 kg/m^3 for TS sample (Table 4).

4.4. Porosity

The porosity of samples was estimated by weighing the dry and saturated sample, similar to the method of *Saad* [1969] and incorporating it into the equation:

$$\varphi_0 = \left(1 - \frac{W_{dry} - W_{sat}}{V}\right) \times 100 \quad (3)$$

Where φ_0 is the porosity %, W_{dry} is the dry weight of the sample and W_{sat} is the saturated weight of the sample gr, and V is the total volume of the sample cm^3. The porosity of the samples ranges between 2.28% in the BC sample to 8.44% in ND sample (Table 4).

5. Discussion

5.1. Pressure Dependency of Matrix Permeability and Microcrack Apertures

Stress dependency of fluid transport and elastic properties of different rock types have been described using an exponential function [e.g. *David et al*., 1994]. γ_k for sandstones, ranges between 0.001-0.02 [*David et al*., 1994], which is lower than that estimated in this study because the nature of permeability is different in ultramafic rocks and sandstones. Permeability in ultramafic rocks is primarily due to microcracks and the main reason for permeability drop is progressive closure of microcracks and fracture network, as opposed to pore collapse in sandstones. Crack closure versus pressure is stronger in the TS and BC samples than in the ND and JC samples, which suggests that permeability in TS and BC may be controlled by critical crack connections rather than by crack aperture. Variations in texture, mineralogy, locality and stress and temperature history of the samples also affects pressure sensitivity coefficient. Alteration and weathering of common surface-derived samples decreases sensitivity of permeability to stress [*Morrow and Lockner*, 1994]. Because the ND and JC samples are more altered than the TS and BC samples, this affect could also explain the lower value of γ_k for the ND and JC samples (Table 1).

Macdonald and Fyfe, [1985] estimates of permeability in partially serpentinized peridotites are an order of magnitude lower than this study. *Hirose and Hayman*, [2008] reports permeability values of about 2 orders of magnitude higher for a serpentinized dunite from IODP hole 1309.

5.2. Permeability-Porosity Correlation

It is common to fit the porosity and permeability correlation to a cubic power law function [e.g. *Kuhn*, 2004]. Understanding the structure and evolution of pore spaces (e.g. packing, compaction, dissolution and precipitation processes), fluid distribution and flow rate is dependent on the power value [*Zhu et al.*, 2007; *Ma and Morrow*, 1996]. The change of porosity resulting from a change in permeability as a function of pressure can be estimated by using:

$$\frac{k}{k_0} = \left(\frac{\varphi}{\varphi_0}\right)^n \tag{5}$$

where φ_0 and k_0 are the porosity and permeability at room pressure, φ is estimated porosity. n characterizes the dependence of permeability on porosity, higher n values represent larger changes in permeability for a given prosity change [*Zhu et al.*, 2007]. Assuming n=3 results in 40-80% decrease in porosity between 0.1 and 30 MPa. Such a rapid decrease in porosity with increasing pressure is unrealistic. Assuming that the density of the sample increases with increasing pressure because of the decrease in porosity, one can use $\frac{P_e - P_0}{K} = \ln\frac{\varphi_0}{\varphi}$, where K is the isothermal bulk modulus of the material. For K=10^5 MPa, then $\frac{\varphi_0}{\varphi}$ ranges between 1.0001-1.0002. The pressure sensitivity is very small. Hence with the change in pressure in the

experiments, the permeability changes much more significantly than would be expected for a small decrease in porosity. Thus an estimate of porosity and permeability from these experiments leads to conclusion that the power law function with powers higher than 3 are applicable to ultramafic rocks.

5.3. Porosity, Density and Degree of Alteration

The porosity of the samples in this study ranges between 2.28% in the BC sample to 8.44% in ND sample. Measured porosities of *Rao and Ramana*, [1974] for pyroxenites range between 0.14 to 4.01%, which fits φ of BC sample. Porosity for partially serpentinized dunites reported by *Rao and Ramana*, [1974] range between 0.25-1.58% and for highly serpentinized dunites range between 2.24-34.51%. High φ estimates in this study could be representative of weathering, alteration and presence of low density minerals such as serpentine and talc.

The density values ranged between 2780 kg/m^3 for ND sample to 3190 kg/m^3 for TS sample. To be able to estimate the degree of alteration in each sample, I use the linear relationship between the degree of alteration β and grain density ρ_g modified from *Escartin et al.* [2001]:

$$\beta = 100 - 100 \times \left(\frac{\rho_g - \rho_{serpentine}}{\rho_{major\ phase} - \rho_{serpentine}}\right) \quad (6)$$

I determined the grain density ρ_g of each sample from the relationship $\rho_g = \frac{\rho}{1-\varphi}$ and assumed density of dunite, enstatite and serpentine are 3330, 3200 and 2550 kg/m^3, respectively. On the basis of equation (6) and the data from Table (4), the estimated degree of alteration for TS, JC and ND are 0.6, 22 and 36% respectively. For BC, it is 7%. These estimates are based on

the assumption that serpentine is the only alteration product. Thus estimated β values in JC, ND and BC are higher than the estimated serpentine fractions in samples (Table 1) because presence of other low density and alteration minerals such as talc, chlorite and actinolite/tremolite have been ignored in the calculation. These minerals have slightly higher densities compared to serpentine. In the TS sample estimated β is slightly lower than observational estimate; this could be as a result of presence of 5-10% orthopyroxene, a high-density mineral. In figure (4) the degree of alteration versus density for this study and what has been reported in *Escartin et al.*, [2001] is plotted. The data fits a linear function with a slope of ~7.25, which can be used to make a rough estimate of the degree of alteration for samples using density.

6. Conclusions

In this study I have measured matrix permeability as a function of effective pressure, and the porosity and density of ultramafic rock samples. The permeability ranged between 4.0E-22 to 3.0E-21at 0.1MPa and decreased by up to an order of magnitude at effective pressures as high as 30 Mpa. The pressure sensitivity coefficient of permeability ranges between 0.05-0.14 MPa^{-1}. The porosity of the samples ranges between 2.28% in a pyroxenite sample to 8.44% in an altered dunite sample. Density values ranged between 2780 kg/m^3 to 3190 kg/m^3. The degree of alteration has an inverse correlation with density, with estimates ranging between 0.6 to 36%. A power law relationship between porosity and permeability shows that the ratio of interconnected porosity to the total is small and the microcracks and fractures have a key role in permeability. These results can be used as a reference for analyzing the pressure sensitivity of deep drill cores in ultramafic rocks.

Acknowledgements

I would like to thank David Lockner and Lee-Grey Boze for helping with sample preparation and data collection. This work was partially supported by NSF grant OCE1131471 to RPL.

7. References

Andrews, D. (2002), A fault constitutive relation accounting for thermal pressurization of pore fluid, *Journal of Geophysical Research*, *107*(B12), 2363, doi:10.1029/2002JB001942.

Bear, J. (1972) *Dynamics of Fluids in Porous Media*, *Elsevier*, New York.

Bickle, M. J., and D. A. Teagle (1992), Strontium alteration in the Troodos ophiolite: implications for fluid fluxes and geochemical transport in mid-ocean ridge hydrothermal systems, *Earth and Planetary Science Letters*, *113*(1), 219-237.

Bjornsson, S., and V. Stefansson (1987), Heat and Mass Transport in Geothermal Reservoirs, in *Advances in Transport Phenomena in Porous Media*, edited by J. Bear and M. Y. Corapcioglu, pp. 143-183, Springer Netherlands.

Bourbie, T., and B. Zinszner (1985), Hydraulic and acoustic properties as a function of porosity in Fontainebleau sandstone, *Journal of Geophysical Research*, *90*(B13), 11524-11532.

Byerlee, J.D., (1968), Brittle-ductile transition in rocks, *Journal of Geophysical Research*, *73*, 4741-4750, doi:10.1016/0191-8141(85)90023-9.

Byerlee, J. D. (1993), Model for episodic flow of high-pressure water in fault zones before earthquakes, *Geology*, *21*(4), 303-306.

Carman, P. (1937), Fluid flow through a granular bed, *Transactions-Institution of Chemical Engineeres*, *15*, 150-166.

Christensen, N. I. (1974), Compressional wave velocities in possible mantle rocks to pressures of 30 kilobars, *Journal of Geophysical Research*, *79(2)*, 407–412.

Christensen, N. I. (1978), Ophiolites, seismic velocities and oceanic crustal structure, *Tectonophysics*, *47*(1), 131-157.

Christensen, N. I. (1996), Poisson's ratio and crustal seismology, *Journal of Geophysical Research*, 101(B2), 3139–3156.

Darnet, M., G. Marquis, and P. Sailhac (2006), Hydraulic stimulation of geothermal reservoirs: fluid flow, electric potential and microseismicity relationships, *Geophysical Journal International*, *166*(1), 438-444.

David, C., T.-F. Wong, W. Zhu, and J. Zhang (1994), Laboratory measurement of compaction-induced permeability change in porous rocks: Implications for the generation and maintenance of pore pressure excess in the crust, *Pure and applied geophysics*, *143*(1-3), 425-456.

Elderfield, H., C. Wheat, M. Mottl, C. Monnin, and B. Spiro (1999), Fluid and geochemical transport through oceanic crust: a transect across the eastern flank of the Juan de Fuca Ridge, *Earth and Planetary Science Letters*, *172*(1), 151-165.

Escartin, J., G. Hirth, and B. Evans (1997), Effects of serpentinization on the lithospheric strength and the style of normal faulting at slow-spreading ridges, *Earth and Planetary Science Letters*, *151*(3), 181-189.

Escartin, J., G. Hirth, and B. Evans (2001), Strength of slightly serpentinized peridotites: Implications for the tectonics of oceanic lithosphere, *Geology*, *29*(11), 1023-102.

Farooqui, M., H. Hou, G. Li, N. Machin, T. Neville, A. Pal, C. Shrivastva, Y. Wang, F. Yang, and C. Yin (2009), Evaluating volcanic reservoirs, *Oilfield Review*, *21*(1), 36-47.

Farough, A., D. E. Moore, D. A. Lockner, R. P. Lowell (2015), Evolution of fracture permeability of ultramafic rocks undergoing serpentinization at hydrothermal conditions: An experimental study, *Geochemistry Geophysics Geosystems*, under review.

Friedman, G. M., and J. E. Sanders (1978), *Principles of sedimentology*, Wiley, New York.

Gamage, K., E. Screaton, B. Bekins, and I. Aiello (2011), Permeability–porosity relationships of subduction zone sediments, *Marine Geology*, *279*(1), 19-36.

Gowd, T.N. (1967), Failure of pyroxenites and peridotites under simple compression, proceeding of 1st Symposium on Upper Mantle Project, *Geophysical Research Board Publications,* Hyderabad, India, 8 (1967), p. 155.

Griffith, E. M., and A. Paytan (2012), Barite in the ocean–occurrence, geochemistry and palaeoceanographic applications, *Sedimentology*, *59*(6), 1817-1835.

Guéguen, Y., and V. Palciauskas (1994), *Introduction to the Physics of Rocks*, P. 294, Princeton University Press, Princeton, NJ.

Hirose, T., and N. W. Hayman (2008), Structure, permeability, and strength of a fault zone in the footwall of an oceanic core complex, the Central Dome of the Atlantis Massif, Mid-Atlantic Ridge, 30°N, *Journal of Structural Geology*, *30*(8), 1060-1071.

Hyndman, R., and M. Drury (1976), The physical properties of oceanic basement rocks from deep drilling on the Mid-Atlantic Ridge, *Journal of Geophysical Research*, *81*(23), 4042-4052.

Hyndman, R., K. Wang, T. Yuan, and G. Spence (1993), Tectonic sediment thickening, fluid expulsion, and the thermal regime of subduction zone accretionary prisms: the Cascadia margin off Vancouver Island, *Journal of Geophysical Research*, *98*(B12), 21865-21876.

Ito, Y., and K. Obara (2006), Very low frequency earthquakes within accretionary prisms are very low stress-drop earthquakes, *Geophysical Research Letters*, *33*, L09302, doi:10.1029/2006GL025883.

Kozeny, J. (1927), About capillaries conducting water in the earth, *Hölder-Pichler-Tempsky*, 136, 271–306.

Kühn, M. (2004). *Reactive flow modeling of hydrothermal systems*. Berlin: Springer-Verlag, doi: 10.1007/b13902.

Lachenbruch, A. H. (1980), Frictional heating, fluid pressure, and the resistance to fault motion, *Journal of Geophysical Research, 85*(B11), 6097-6112.

Lowell, R. P., Circulation in fractures, hot springs, and convective heat transport on mid-ocean ridge crests, *Geophysical Journal of the Royal Astronomical Society,40*, 351–365, 1975.

Ma, S., and N. R. Morrow (1996), Relationships between porosity and permeability for porous rocks, *paper presented at International symposium of the Society of Core Analysts*, September 8-10, 1996.

Macdonald, A., and W. Fyfe (1985), Rate of serpentinization in seafloor environments, *Tectonophysics, 116*(1), 123-135.

Milsch, H., A. Seibt, and E. Spangenberg (2009), Long-term petrophysical investigations on geothermal reservoir rocks at simulated in situ conditions, *Transport in Porous Media*, *77*(1), 59-78.

Morrow, C., and D. Lockner (1994), Permeability differences between surface-derived and deep drillhole core samples, *Geophysical Research Letters*, *21*(19), 2151-2154.

Morrow, C. A., D. A. Lockner, D. E. Moore, and S. Hickman (2014), Deep permeability of the San Andreas Fault from San Andreas Fault Observatory at Depth (SAFOD) core samples, *Journal of Structural Geology*, *64*, 99-114.

Paterson, M. (1983), The equivalent channel model for permeability and resistivity in fluid-saturated rock—a re-appraisal, *Mechanics of Materials*, *2*(4), 345-352.

Pruess, K. (2004), The TOUGH codes—a family of simulation tools for multiphase flow and transport processes in permeable media, *Vadose Zone Journal*, *3*(3), 738-746

Raleigh, C., and M. Paterson (1965), Experimental deformation of serpentinite and its tectonic implications, *Journal of Geophysical Research*, *70*(16), 3965-3985.

Rao, M. V. M. S., Ramana, Y. V. (1974), Dilatant behaviour of ultramafic rocks during fracture, *International Journal of Rock Mechanics and Mineral Science*, *11*,193-203.

Saad, A. H. (1969), Magnetic properties of ultramafic rocks from Red Mountain, California, *Geophysics*, *34*(6), 974-987.

Schutter, S. R. (2003), Hydrocarbon occurrence and exploration in and around igneous rocks, *Geological Society, London, Special Publications*, *214*(1), 7-33.

Shi, Y., and C. Y. Wang (1986), Pore pressure generation in sedimentary basins: overloading versus aquathermal, *Journal of Geophysical Research*, *91*(B2), 2153-2162.

Shimada, M., Cho, A., and Yukutake, H., 1983, Fracture strength of dry silicate rocks at high confining pressures and activity of acoustic emission: *Tectonophysics*, *96*, 159-172.

Sibson, R. H. (1994), Crustal stress, faulting and fluid flow, *Geological Society, London, Special Publications*, *78*(1), 69-84.

Sleep, N. H., and M. L. Blanpied (1994), Ductile creep and compaction: a mechanism for transiently increasing fluid pressure in mostly sealed fault zones, *Pure and applied geophysics*, *143*(1-3), 9-40.

Suzuki, T., and T. Yamashita (2009), Dynamic modeling of slow earthquakes based on thermoporoelastic effects and inelastic generation of pores, *Journal of Geophysical Research*, *114*, B00A04, doi:10.1029/2008JB006042.

Tanikawa, H., S. Managi, and C. M. Lwin (2014), Estimates of lost material stock of buildings and roads due to the Great East Japan Earthquake and tsunami, *Journal of Industrial Ecology*, *18*(3), 421-431.

Taron, J., and D. Elsworth (2009), Thermal–hydrologic–mechanical–chemical processes in the evolution of engineered geothermal reservoirs, *International Journal of Rock Mechanics and Mining Sciences*, *46*(5), 855-864.

Thompson, A., A. Katz, and C. Krohn (1987), The microgeometry and transport properties of sedimentary rock, *Advances in Physics*, *36*(5), 625-694.

Tiab, D., and E. C. Donaldson (2011), *Petrophysics: theory and practice of measuring reservoir rock and fluid transport properties*, Gulf Publishing Company, Houston, TX.

Walsh, J. (1965), The effect of cracks on the compressibility of rock, *Journal of Geophysical Research*, *70*(2), 381-389.

Walsh, J., and W. Brace (1984), The effect of pressure on porosity and the transport properties of rock, *Journal of Geophysical Research*, *89*(B11), 9425-9431.

Zhu, W., T. F. Wong (1997), The transition from brittle faulting to cataclastic flow: Permeability evolution, *Journal of Geophysical Research*, 102, 3027–3041.

Zhu, W., M. K. Tivey, H. Gittings, and P. R. Craddock (2007), Permeability-porosity relationships in seafloor vent deposits: Dependence on pore evolution processes, *Journal of Geophysical Research*, *112*(B5), B05208, doi:10.1029/2006JB004716.

8. Figures

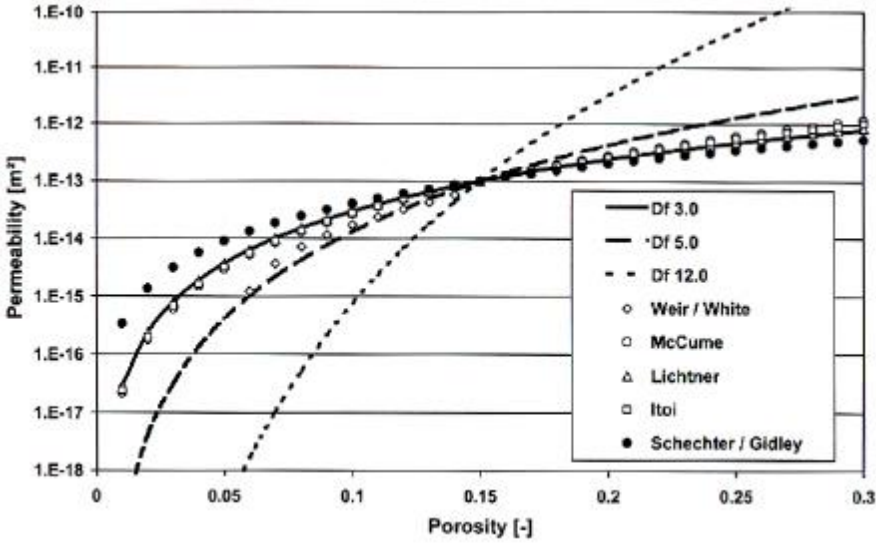

Figure (1): Porosity-permeability relationship, assuming an initial porosity of 0.15 and an initial permeability of 10^{-13} m^2. The solid line is for *n*=3 [from *Kühn*, 2004]

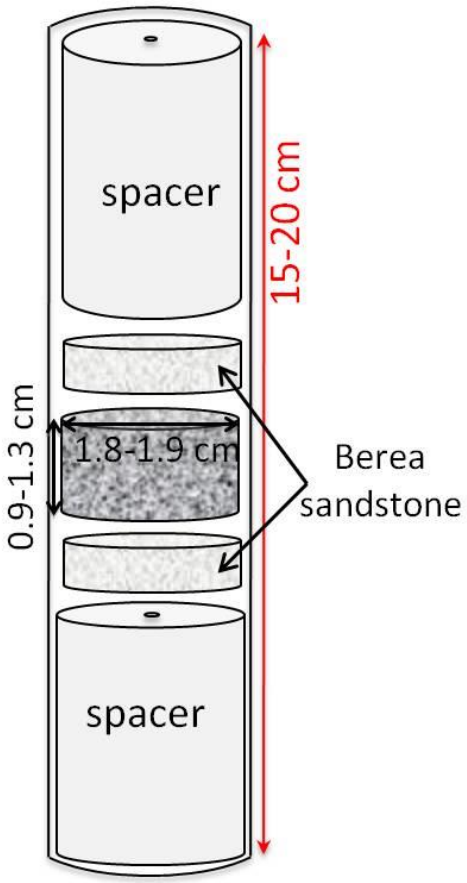

Figure (2): Sample assembly

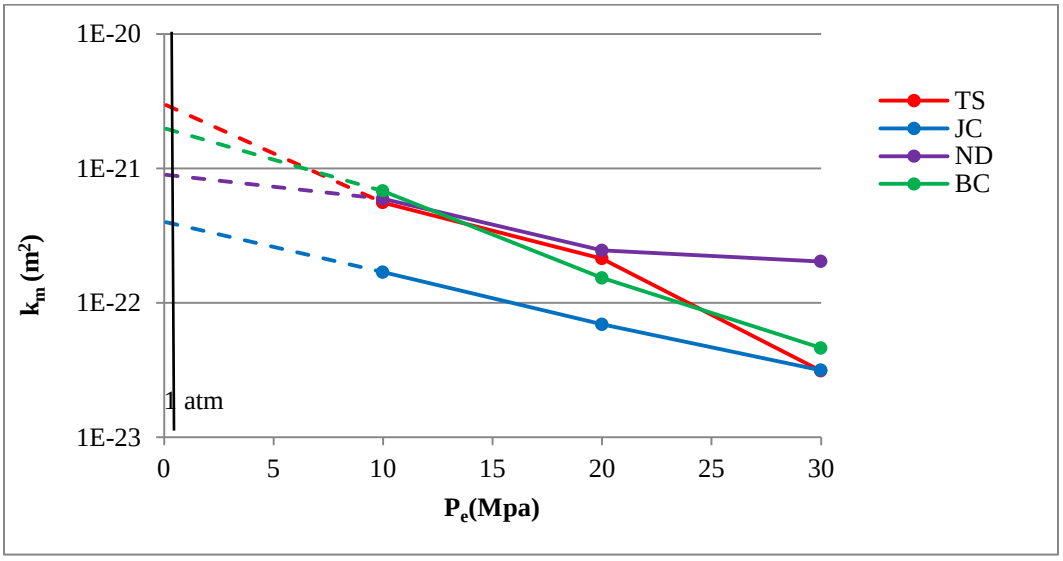

Figure (3): Pressure dependency of matrix permeability k_m. Values of permeability at 1 atm (0.1 MPa) have been extrapolated (dashed lines) based on a best fit exponential function.

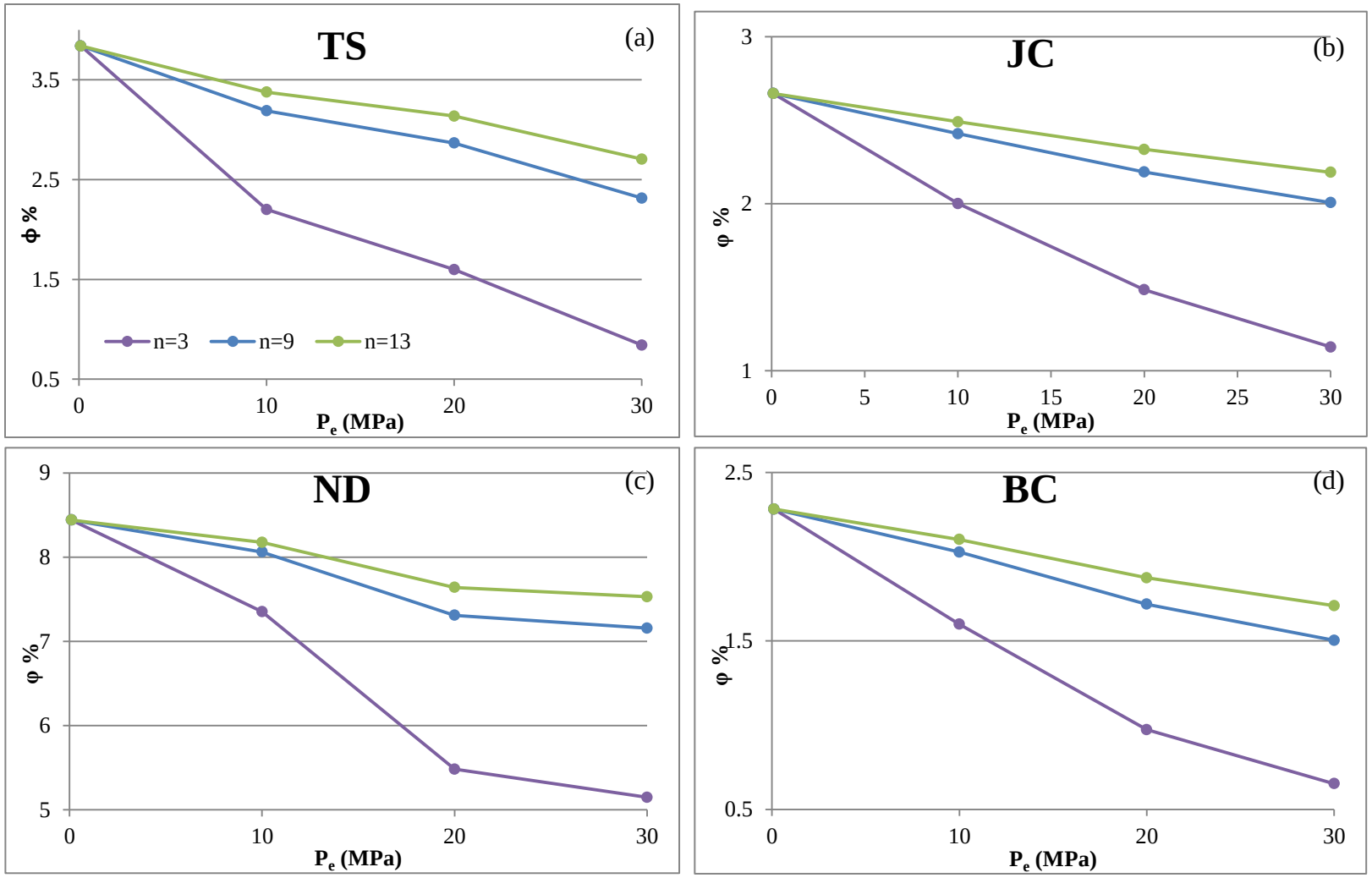

Figure (4): Estimated pressure dependency of porosity from equation (4). (a) TS, (b) JC, (c) ND, (d) BC

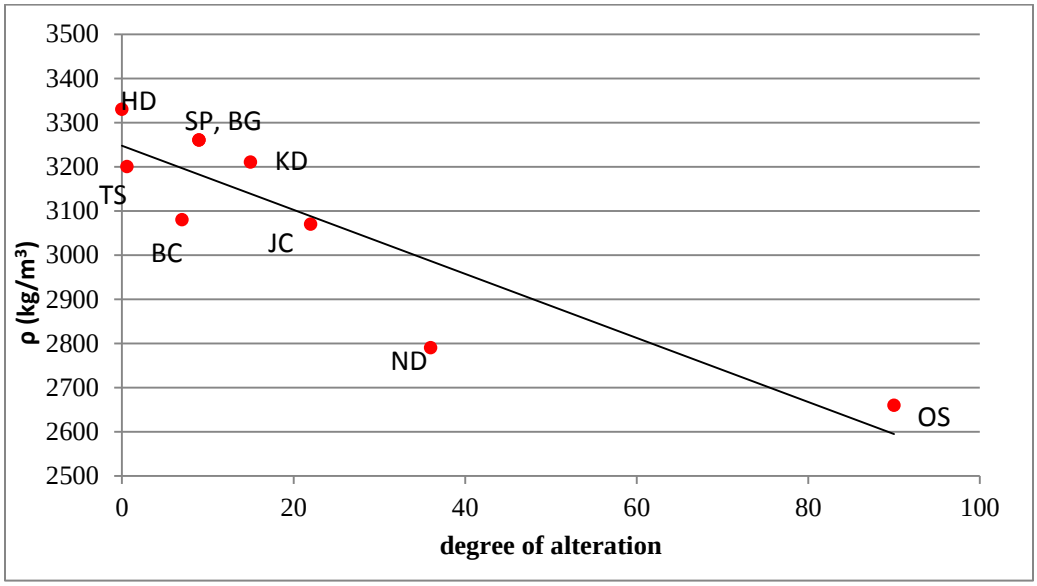

Figure (5): Measured density vs. estimated degree of alteration for the samples from this study and *Escartin et al.*, [2001]

9. Tables

Table (1): Description of the samples used for the experiments.

Sample		Locality	Average grain size mm	Mineral assemblage	
				Major phase* (~80-90%)	Other phases (~10-20%) **
Dunite	TS	Twin Sisters, WA	0.2-5	Olivine ($Mg_{1.8}$, $Fe_{0.2}$)	Serpentine(1-2%), opx (5-10%), chromium spinel (<2%)
	JC	Jackson County, NC	0.1-0.3	Olivine ($Mg_{1.7}$, $Fe_{0.3}$)	Serpentine(2-4%), talc (<1%), actinolite/tremolite (2-5%), chlorite (<1%), chromium spinel (2-5%),
	ND	Spruce Pine, NC	0.1-0.6	Olivine ($Mg_{1.8}$, $Fe_{0.2}$)	Serpentine(5-8%), talc (2%), chlorite (2%), actinolite/tremolite (2%)
Pyroxenite	BC	east of Bushveld complex, South Africa	0.05-0.2	Orthopyroxene ($Mg_{0.56}$, $Fe_{0.44}$)	Serpentine (2-4%), plagioclase (2-4%), talc (2%), olivine (5%)

* Compositions are provided using XRD, Rigaku's PDXL software (version 1.8)

** Percentage of alteration products are estimated by optical mineralogy

Table (2): Experimental conditions for both intact and fractured samples

Experimental conditions	Intact experiments
T ˚C	23-25
Pc MPa	12, 22, 32
Average P_p MPa	2
P_e MPa	10, 20, 30
Initial pore pressure difference across the sample MPa	4

Table (3): Fitted equations for intact permeability of each sample

Sample	*Exponential fit*	R^2	k_{m0} m^2	γ_k MPa^{-1}
TS	$y = 3E\text{-}21e^{-0.144x}$	0.96	3E-21	0.144
JC	$y = 4E\text{-}22e^{-0.084x}$	0.99	4E-22	0.084
ND	$y = 9E\text{-}22e^{-0.053x}$	0.87	9E-22	0.053
BC	$y = 2E\text{-}21e^{-0.134x}$	0.99	2E-21	0.134

Table (4): Measured dry and saturated weight of the samples, estimated porosity, density and grain density at 1 atm

Sample	Dry weight g	Submerged saturated weight g	ρ kg/m^3	φ %	ρ_g kg/m^3
TS	5.91	4.13	3200	3.84	3320
JC	8.55	5.84	3070	2.66	3160
ND	7.16	4.81	2790	8.44	3040
BC	11.51	7.86	3080	2.28	3150

Table (5): Estimated degree of alteration in the samples of this study compared to that reported by *Escartin et al.*, [2001]

	ρ kg/m^3	β	Reference
Balsam gap Dunite (BG)	3260	9	*Escartin et al.*, 2001
Kukes Dunite (KD)	3210	15	*Escartin et al.*, 2001

Horoman Dunite (HD)	3330	0	*Shimada et al.*, 1987
Spruce Pine Dunite (SP)	3260	9	*Byerlee, 1968*
Oceanic serpentinite (OS)	2660	>90	*Escartin et al.*, 1997a
Twin Sisters Dunite (TS)	3200	0.6	This study
Jackson County Dunite (JC)	3070	22	This study
Newdale Dunite (ND)	2790	36	This study
Bushveld Complex pyroxenite(BC)	3080	7	This study